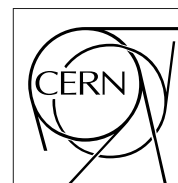


The Compact Muon Solenoid Experiment

CMS Note

Mailing address: CMS CERN, CH-1211 GENEVA 23, Switzerland



May 15, 2006

CMS Sensitivity to Dijet Resonances

Kazim Gumus and Nural Akchurin

Texas Tech University, Lubbock, TX, USA

Selda Esen

Cukurova University, Adana, Turkey

Visitor at Fermilab, Batavia, IL, USA

Robert M. Harris

Fermilab, Batavia, IL, USA

Abstract

We estimate CMS sensitivity to narrow resonances in the dijet final state. The generic signal shape and QCD background are presented as a function of dijet mass for jet pseudorapidity in the region $|\eta| < 1$. Statistical and systematic uncertainties are estimated for integrated luminosities of 100 pb^{-1} , 1 fb^{-1} , and 10 fb^{-1} and a realistic trigger table including multiple thresholds and prescales for jets. The cross section for a dijet resonance that CMS can expect to discover at 5σ significance or exclude at 95% confidence level is presented. We compare these cross section sensitivities with the expected cross section from models of excited quarks, axigluons, colorons, E_6 diquarks, color octet technirhos, W' , Z' , and Randall-Sundrum gravitons to determine the masses for which we expect to be able to discover or to exclude these models of dijet resonances.

1 Introduction

We will search for processes producing narrow resonances, X , decaying to two jets as illustrated in fig. 1: $pp \rightarrow X \rightarrow \text{jet} + \text{jet}$ (inclusive). This section describes the motivation and general strategy for the search and concludes with a brief description of the models of dijet resonances we will consider.

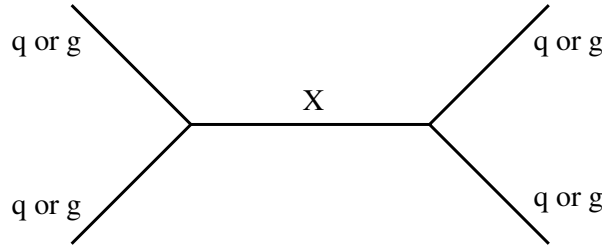


Figure 1: Feynman diagram for a dijet resonance. The initial state and final state both contain two partons (quarks, antiquarks or gluons) and the intermediate state contains an s -channel resonance X .

1.1 Motivation

Our experimental motivation is that LHC is a parton-parton collider in a previously unexplored energy region. If new parton-parton resonances exist then the LHC will produce them copiously. These resonances must also decay to partons giving two jets in the final state. The experimental motivation to search for dijet resonances is intuitively obvious.

The current theoretical motivation to search for dijet resonances is broad. Dijet resonances are found in models that address some of the most profound questions of particle physics beyond the Standard Model, the Higgs mechanism, or supersymmetry:

- **Why are there quark flavors?**
The theoretical ideas behind extended technicolor and topcolor assisted technicolor at least attempt to address this difficult question, and the models predict the color octet technirho and colorons.
- **Why are quarks arranged in generations?**
Compositeness has successfully explained repeating patterns in the past: the periodic table, hadron multiplets, etc. When composite quarks are struck by a gluon they can be excited to a higher state, and these excited quarks can then decay in the same fashion.
- **Why are there so many different forces?**
Grand unified theories postulate that the electroweak and strong forces come from a single interaction at much higher energies. These theories generally predict an extra heavy Z boson, and occasionally predict an extra heavy W boson.
- **How do we unify gravity with the other forces?**
Superstring theory employs both supersymmetry and string theory and attempts to unify Gravity with the other forces. Some superstring models predict that at low energies the standard model originates from the E_6 gauge group that contains diquarks.

- **Why is gravity so weak?**

Recent models postulate that the strength of gravity is reduced by leaking into an extra dimension. Theoretically they are very compelling because they solve the hierarchy problem of the separation between the Planck scale of unification and the TeV scale of physical phenomena. The Randall-Sundrum model predicts massive gravitons.

That the discovery of a dijet resonance would provide support for any of these existing models, and thereby help answer any one of these questions, should be sufficient motivation to search. However, there is also the more interesting possibility that we will enter an era where experimental discovery leads theoretical ideas, much like we saw in the 1960s and 70s. The idea for a completely new model of physics, which answers one or all of these questions, could originate from the discovery of a dijet resonance.

1.2 General Strategy

Experimental searches in the dijet channel are challenging because of the large QCD background and often limited dijet mass resolution. Nevertheless, high statistics in the dijet sample allow exclusions of cross sections that are a small fraction of the QCD dijet cross section. Also, new particles with a natural width significantly smaller than the measured dijet mass resolution should all appear as a dijet mass resonance of the same line shape in the CMS detector. We model the resonance shape for a single type of particle decaying to dijets and we use that shape to generically search for any narrow dijet resonance in the dijet mass distribution. If we find no resonances we determine the 95% CL upper limit on the cross section, which can then be compared to the dijet cross section for any model of narrow resonance to determine the mass limits. Similarly, if we discover a new particle, the measured cross section for that particle can be compared to the expected cross section for any particular model of narrow resonance to help determine the origin of the particle discovered.

In this note we estimate the narrow dijet resonance cross sections that can be excluded at 95% CL or discovered with 5σ significance. These cross section sensitivities are generic, and can be applied to constrain the cross section of any model of narrow dijet resonances. We compare our cross section sensitivities to the predicted cross section of seven benchmark models of narrow dijet resonances, and determine which models can be discovered or excluded.

The strategy is purely empirical. It is simple bump hunting in the dijet channel. We want to avoid bias toward any particular theoretical model. Our analysis is not tuned on any particular model of new physics, and is therefore able to discover or constrain any model that yields narrow dijet resonances.

1.3 Dijet Resonance Models

There are many classes of new particles that decay to two partons. The branching fraction in the dijet channel is often larger than channels containing leptons or electroweak gauge bosons. In Figure 2, we show the cross section times branching ratio calculated to lowest order for some models. The calculation and the details of the models are discussed in Appendix A. Here we introduce the models in order of descending cross section at low mass, say a few words about the relative cross section of each model, and explicitly list the partons involved in production and decay. Excited states of composite quarks [1] are strongly produced giving large cross sections ($qg \rightarrow q^*$). Axigluons [2] or colorons [3] from an additional color interaction are also strongly produced, but require an antiquark in the initial state ($q\bar{q} \rightarrow A$ or

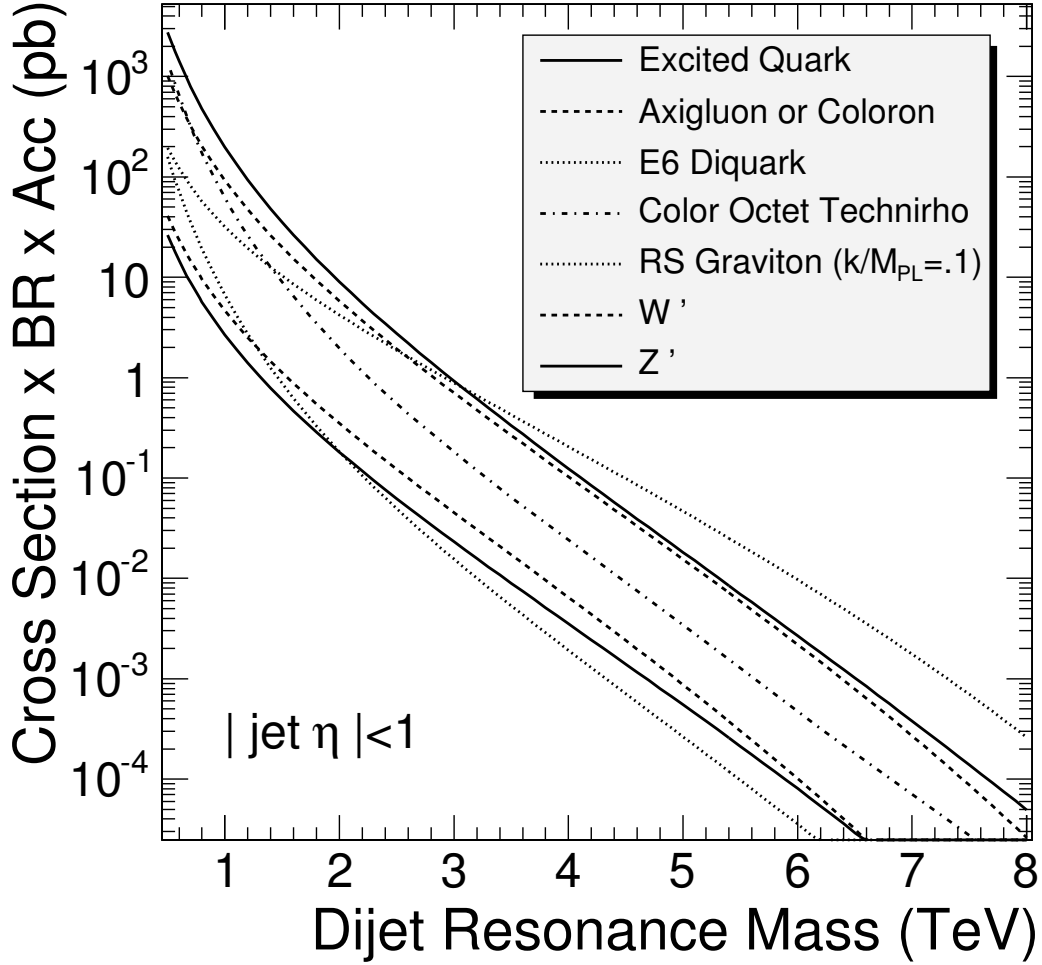


Figure 2: The cross section for dijet resonances with $|\eta| < 1$ is shown as a function of resonance mass for the following models: excited quarks (upper solid), axigluons or colorons (upper dashed), E_6 diquarks (upper dotted), color octet technirhos (dot-dashed), Randall-Sundrum gravitons (lower dotted), W' (lower dashed) and Z' (lower solid).

C) slightly reducing the cross section compared to excited quarks. Diquarks [4] from superstring inspired E_6 grand unified models are produced with electromagnetic coupling from the valence quarks of the proton ($ud \rightarrow D$). The cross section for E_6 diquarks at high mass is the largest of all the models considered, because at high parton momentum the probability of finding a quark in the proton is significantly larger than the probability of finding a gluon or antiquark. Color octet technirhos [5] from technicolor are produced for either gluons or quark-antiquark pairs in the initial state through a vector-dominance model of mixing between the gluon and the technirho ($q\bar{q}, gg \rightarrow g \rightarrow \rho_{T8}$). Randall Sundrum gravitons [6] from a model of large extra dimensions are produced from gluons or quark-antiquark pairs in the initial state ($q\bar{q}, gg \rightarrow G$). Heavy W bosons [7] inspired by left-right symmetric grand unified models have electroweak couplings and require antiquarks for their production ($q_1\bar{q}_2 \rightarrow W'$), giving small cross sections. Heavy Z bosons [7] inspired by grand-unified models are widely anticipated by theorists, but they are electroweakly produced, and require an antiquark in the initial state ($q\bar{q} \rightarrow Z'$), so their production cross section is around the lowest of the mod-

els considered. Published lower limits from CDF [8] and D0 [9] on the mass of these models in the dijet channel are listed in table 1.

q^*	A or C	D	ρ_{T8}	W'	Z'	G
0.78	0.98	0.42	0.48	0.8	0.6	-

Table 1: Published lower limits in TeV on the mass of new particles considered in this analysis. These 95% confidence level exclusions are from the Tevatron and are the best published limits in the dijet channel that use a similar technique as presented in this note. Exclusions from the di-lepton channel are better for W' , Z' and G . Exclusions from the di-leptoquark channel are better for ρ_{T8} . Exclusions from the dijet channel using the angular distribution are better for A or C . These are the best exclusions of any channel for q^* or D .

2 Jets and QCD

Here we consider jet reconstruction, dijet analysis, and the QCD background to dijet resonances. Inclusive dijet production ($pp \rightarrow 2 \text{ jets} + X$) is the LHC process with the largest cross section. It is dominated by the $2 \rightarrow 2$ QCD scattering of partons (quarks, antiquarks, and gluons) in which there are only partons in the initial, intermediate and final states. It is the only background we consider at this time. The measurement of the dijet mass distribution at CMS, including a detailed discussion of the trigger, has been previously presented [10]. In this section we first discuss jet reconstruction and then review the results on the dijet mass distribution.

2.1 Jet Reconstruction and Dijet Analysis

Jets are reconstructed as localized energy depositions in the CMS calorimeters arranged in a projective tower geometry (EcalPlusHcalTowers). The jet energy E is defined as the scalar sum of the calorimeter tower energies inside a cone of radius $R = \sqrt{(\Delta\eta)^2 + (\Delta\phi)^2} = 0.5$, centered on the jet direction. The jet momentum \vec{p} is the corresponding vector sum of energies, with the vector pointing in the tower direction. The jet transverse energy is $E_T = E \sin \theta$, and the jet transverse momentum is $p_T = p \sin \theta$, where θ is the angle between the jet momentum and the proton beam. Both the jet energy and momentum are corrected back to the particles in the jet cone originating from the hard interaction excluding pileup.

This paragraph discusses some of the details of the jet reconstruction used for both signal and background. EcalPlusHcalTowers were reconstructed with the default CMS algorithm which cut at 0.5 GeV on the energy in each HCAL compartment. Offline jets were reconstructed with the default CMS algorithm [11]: iterative cone algorithm, a cone size of $R = 0.5$, no seed threshold, 0.5 GeV E_T tower threshold, and E-scheme method of constructing jet four vectors. All reconstructed jets with $p_T > 10$ GeV were written to a root tree [12], along with a single multiplicative correction factor for the offline jet Lorentz vector [10]. The correction is designed to give a Lorentz vector from the particles in a jet cone of radius $R = 0.5$ before pileup. The correction depends on reconstructed jet p_T and η . For jets in the region $|\eta| < 1$ on average a reconstructed p_T of 75 GeV was corrected by 33% to give 100 GeV, a p_T of 430 GeV by 16% to give 500 GeV, and a p_T of 2.8 TeV by 7% to give 3.0 TeV corrected jet p_T .

We define the dijet system as the two jets with the highest p_T in an event (leading jets) and define the dijet mass $m = \sqrt{(E_1 + E_2)^2 - (\vec{p}_1 + \vec{p}_2)^2}$. We select events in which the leading

jets each have $|\eta| < 1$. This keeps practically all of the jet energy within the barrel region of the CMS calorimeter. This cut also enhances our sensitivity to new physics, produced at low $|\eta|$, compared to the predominantly t -channel processes from the QCD background. The value of the $|\eta|$ cut is the same as our other analyses [10, 15] and was intended to be similar to prior resonance searches at the Tevatron [8, 9]. Optimization of the $|\eta|$ cut for the LHC has not been done, but we expect from Tevatron experience that the cut is reasonably close to the optimal value for an analysis that uses a single value of the cut for all values of dijet mass. As in the dijet mass analysis [10], in all plots that are a function of dijet mass, we plot in bins of width equal to the expected mass resolution, discussed in section 3.2.

2.2 Trigger and Dijet Mass Distribution

In table 2 we list the dijet mass range that we analyze from each trigger. The lower value of the mass range is the lowest value of dijet mass for which the trigger is fully efficient [10]. The upper value of the mass range is the mass value where the next highest threshold trigger becomes fully efficient. For the unprescaled trigger, where there is no next highest threshold, there is no upper mass value. The efficiency of each trigger will be measured using the next trigger in each table with a lower threshold. Since there is no trigger with E_T threshold beneath the path labeled *Low* in any of the tables, we do not know how the trigger efficiency for the *Low* path will be measured, and therefore we do not use the *Low* path to measure the dijet mass.

Path	L1				HLT		ANA
	E_T Cut (GeV)	Unpres. Rate (KHz)	Prescale (N)	Presc. Rate (KHz)	E_T Cut (GeV)	Rate (Hz)	Dijet Mass (TeV)
Triggers for $\mathcal{L} = 10^{32} \text{ cm}^{-2} \text{ s}^{-1}$ and integrated luminosity = 100 pb $^{-1}$							
High	140	0.044	1	0.044	250	2.8	>0.67
Med	60	3.9	40	0.097	120	2.4	0.33-0.67
Low	25	2.9×10^2	2,000	0.146	60	2.8	None
Triggers for $\mathcal{L} = 10^{33} \text{ cm}^{-2} \text{ s}^{-1}$ and integrated luminosity = 1 fb $^{-1}$							
Ultra	270	0.019	1	0.019	400	2.6	>1.13
High	140	0.44	10	0.044	250	2.8	0.67-1.13
Med	60	39	400	0.097	120	2.4	0.33-0.67
Low	25	2.9×10^3	20,000	0.146	60	2.8	None
Triggers for $\mathcal{L} = 10^{34} \text{ cm}^{-2} \text{ s}^{-1}$ and integrated luminosity = 10 fb $^{-1}$							
Super	450	0.014	1	0.014	600	2.8	>1.80
Ultra	270	0.19	10	0.019	400	2.6	1.13-1.80
High	140	4.4	100	0.044	250	2.8	0.67-1.13
Med	60	3.9×10^2	4,000	0.097	120	2.4	0.33-0.67
Low	25	2.9×10^4	200,000	0.146	60	2.8	None

Table 2: The single jet trigger table previously proposed [10], showing path names, trigger thresholds in corrected E_T , prescales, estimated rates at L1 and HLT for three different luminosity scenarios, and here we also list the corresponding range of corrected dijet mass used in this analysis. The trigger in the Low path is not used to measure the dijet mass.

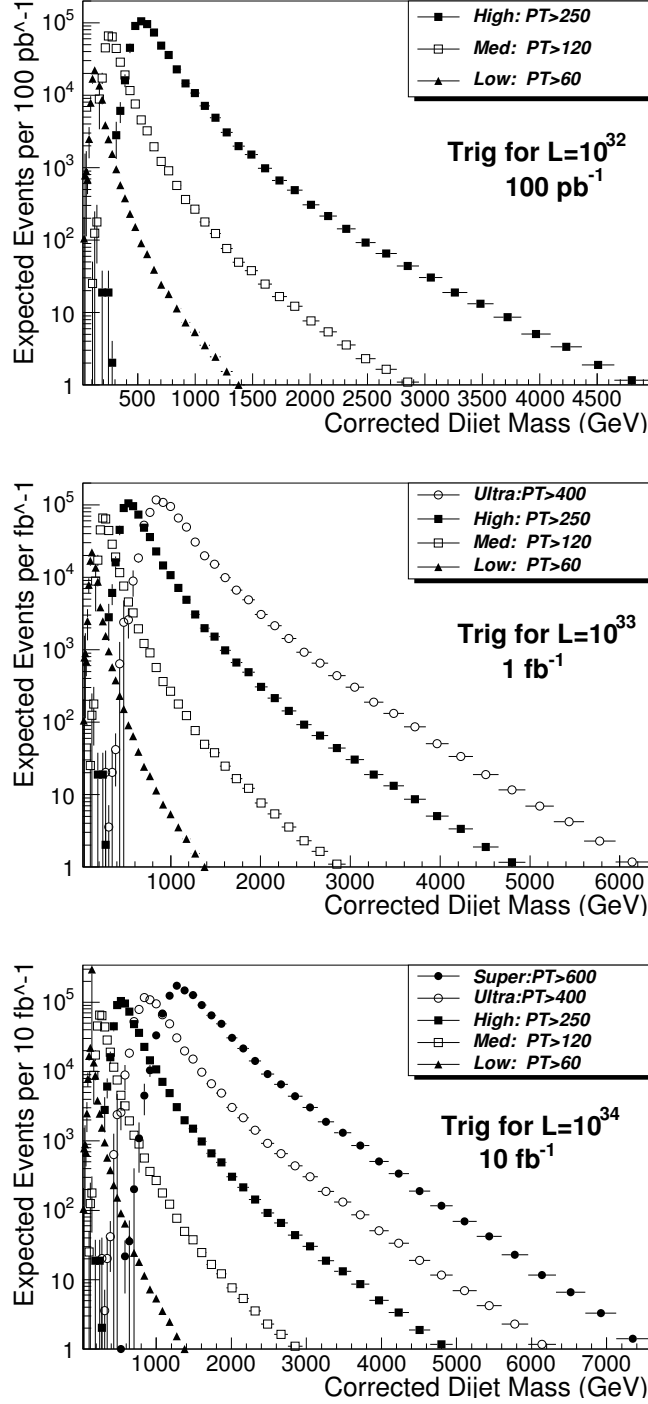


Figure 3: Rate of jet trigger as a function of dijet mass. The 3 plots correspond to 3 luminosity scenarios in the trigger table 2. Each plot shows the rate as a function of dijet mass for multiple triggers with the listed HLT p_T thresholds and prescales.

In figure 3 from reference [10] we show the rate as a function of dijet mass that result from our triggers and prescales. For any given luminosity scenario, the prescales introduce the saw-tooth structure in the rates, producing multiple falling distributions. For integrated luminosities of 100 pb^{-1} , 1 fb^{-1} and 10 fb^{-1} table 2 shows that we employ 2, 3, and 4 triggers for the measurement, and figure 3 shows a corresponding number of falling distributions. This is the rate of the QCD background we expect to measure.

The triggers presented are a reasonable strategy to follow if we have no prior indication of a resonance at any particular value of mass. If a resonance were observed in any other channel, for example di-leptons, and that mass were within our prescaled trigger, it would be natural to reduce the prescales to concentrate on the mass range of interest. We could increase our HLT rate within the desired mass range at the expense of other mass ranges and also use more of the total HLT bandwidth at the expense of other triggers. A factor of 10 higher rate is conceivable while still writing out all the data. If writing out the data is not required, but instead the analysis is done completely in HLT and only a summary of the data or the result is written out, we then are only limited by the L1 total bandwidth. Since the L1 total bandwidth is roughly 1000 times higher than the HLT bandwidth, the rate could be as much as 1000 times higher if this aggressive strategy were employed. However, it would be harder to understand the systematic uncertainties on a dijet resonance analysis performed inside the HLT trigger.

The measured cross section as a function of dijet mass before prescaling is shown in figure 4 taken from reference [10]. The prescaled triggers allow us to measure mass down to 330 GeV, or even smaller if we can understand the efficiency of the lowest threshold trigger. The mass measured with the prescaled triggers will allow us to connect to dijet masses measured at the Tevatron [13, 14]. Since there has been no new physics beyond the standard model discovered in dijets at the Tevatron, this mass region can be a control region of the CMS measurement which defines the QCD background to searches for new physics with dijets.

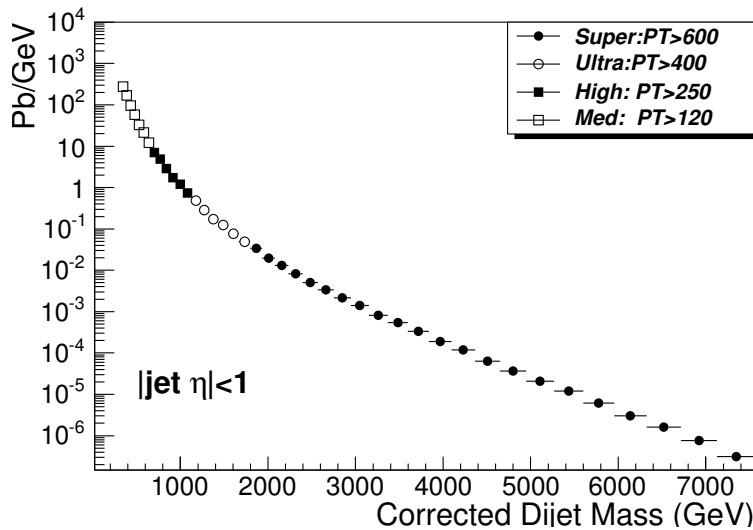


Figure 4: QCD differential cross section vs. dijet mass, showing the contributing jet triggers with different symbols, listed with their path names and p_T thresholds at HLT in the legend.

2.3 Systematic Uncertainties

In figure 5 from reference [10] we summarize the systematic uncertainties on the dijet cross section of the QCD background. Note that the dominant systematic uncertainty in the cross section results from a 5% uncertainty in the jet energy scale. Adding the other systematic uncertainties in quadrature with this systematic does not appreciably change its value. We will use the jet energy scale systematic as an estimate of our uncertainty on the QCD background in this analysis.

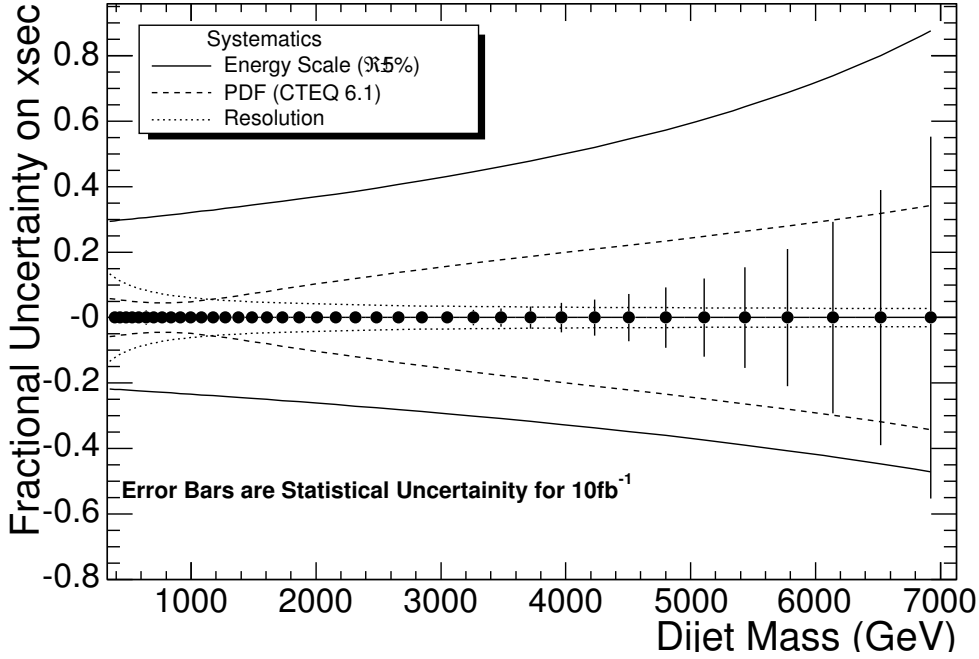


Figure 5: Systematic uncertainty on the dijet cross section due to jet energy scale (solid curve), parton distributions (dashed curve), and calorimeter energy and η resolution (dotted curve) are compared to the statistical uncertainties for 10 fb^{-1} (error bars).

3 Dijet Resonances

3.1 Simulation of Narrow Dijet Resonances

We have performed a full simulation of the inclusive process $pp \rightarrow Z' \rightarrow q\bar{q}$ in the CMS detector at the three resonance masses 0.7, 2.0 and 5.0 TeV. We used the same basic configuration of generation, simulation, and reconstruction as was employed for DC04 production of the QCD background [10] but we changed the process from QCD to a Z' . The generator was Pythia, with Z' allowed to decay to $q\bar{q}$ only. During digitization each Z' event was mixed with the number of minimum bias events corresponding to the anticipated number of multiple interactions for a luminosity of $2 \times 10^{33} \text{ cm}^{-2} \text{ s}^{-1}$. The same number of pileup interactions used when forming the jet corrections. All reconstructed jets with $p_T > 10 \text{ GeV}$ were written to a root tree [12], along with a single multiplicative correction factor for the offline jet Lorentz vector [10]. We required the two leading jets in the event to each have $|\eta| < 1$ and we measured the dijet mass distribution of the Z' resonances using the same bins as

for the QCD background. For these dijet mass values the jet corrections removed practically all effects of pileup, so these dijet mass distributions are applicable for all the luminosities considered.

In the top left plot of Fig. 6 we show the simulated differential cross section as a function of dijet mass for a Z' decaying to dijets compared with the QCD cross section discussed in the previous section. It is clear that this Z' model has a low rate compared to QCD and will be difficult to discover. In the top right plot of Fig. 6 we show the same signal shape but with the total cross section appropriate for an excited quark, where the signal to background ratio is much better. As discussed in the next section, the signal shape has a Gaussian core and a long tail to low mass. In the bottom plot of Fig. 6 we also show the ratio of dijet resonance signals to the QCD background, which illustrates what regions of the signal line shape are most relevant for this analysis. The ratio shows that the long tail to low mass is effectively "lost" in the large QCD background at low mass, and we will only be sensitive to the Gaussian part of the distribution in the search. In section 6 we will discuss how different assumptions about how much of the resonance cross section goes into the tail and how much into the core affect our final sensitivity to resonances.

In the bottom plot of Figure 6 we demonstrate the size of the signal for excited quarks and E_6 diquarks compared to the QCD background and its statistical uncertainty. It is clear that we will be sensitive to such large signals for strongly produced dijet resonances.

3.2 Narrow Dijet Resonance Shapes

The simulated shape of a 2 TeV narrow dijet resonance in CMS is shown in Figure 7. The shape is composed of a Gaussian distribution from jet energy resolution and a long tail to low dijet mass. The Gaussian component can be seen from a fit to the peak and the high mass edge of the resonance. Figure 7 also shows that the measured RMS, σ , of the Gaussian component and its variation with resonance mass, M . The variation of the Gaussian component of the dijet mass resolution is well fit by the functional form $\sigma/M = 0.045 + 1.3/\sqrt{M}$ where M is given in GeV. We used this expression for the dijet mass resolution to define the mass bins, all of width 1σ , in our plots of dijet mass in this note and in two preceding notes [10, 15]. Since there is a tail to low mass which is not included in this expression, our mass bins are really a little smaller than the non-Gaussian "resolution" of the full line shape.

The long tail to low mass comes predominately from final state QCD radiation. When a hard gluon is radiated off of a final state parton it can produce final state particles far away from the final state parton. The energy from these particles will not be inside the jet cones of the two leading jets in the event. It is lost from the reconstructed dijet mass and produces a low mass tail. Radiation modifies the shape of the resonance, but there is no reduction in overall rate of accepted events, since our measurement is inclusive. For the 5 TeV Z' in Fig. 6 there is also a component of the very long tail at low mass which is from parton distributions. There are many partons at low momentum which multiply the rate of the long relativistic Breit-Wigner tail of a very heavy Z' , giving a cross section at low mass that is non-negligible compared to the cross section at the input pole mass. The low mass tail, and associated systematic uncertainties, will be discussed in greater detail in section 6. Here we simply note that the QCD background at low mass completely overwhelms the low mass tail as can be seen from the ratio of signal to background in Figure 6. The signal to background ratio of any narrow resonance will have this shape in the CMS detector.

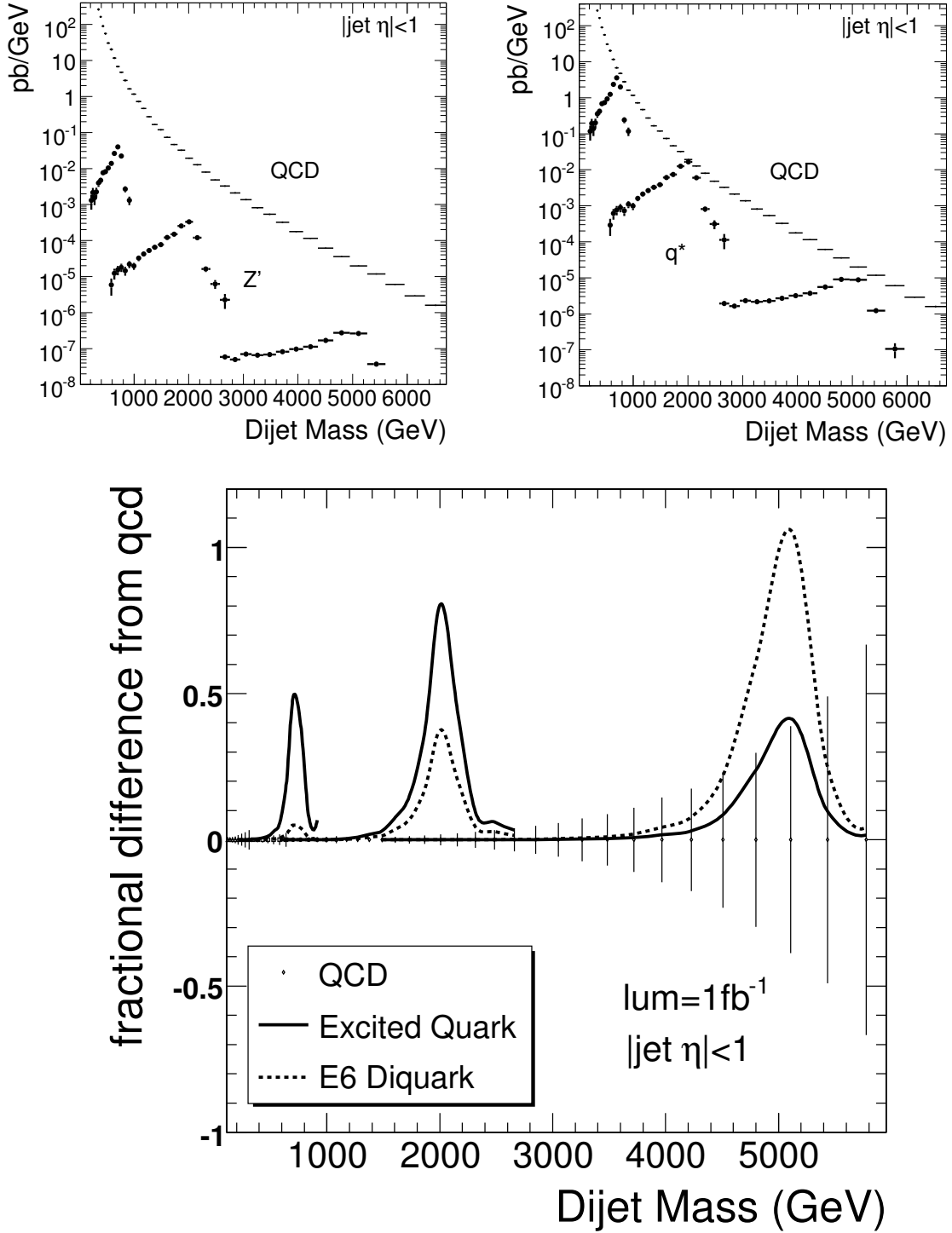


Figure 6: Top Left) The differential cross section as a function of dijet mass for the QCD background and three Z' signals with a mass of 0.7, 2, and 5 TeV/c^2 . Top Right) An excited quark signal using the same resonance masses and shapes as the left plot, but the appropriate total cross section for an excited quark. Bottom) Using the same resonance masses and shapes as above we show the fractional difference between an excited quark (solid curve) or an E6 diquark (dashed curve) and the QCD dijet background compared to the QCD statistical error (vertical lines) for 1 fb^{-1} .

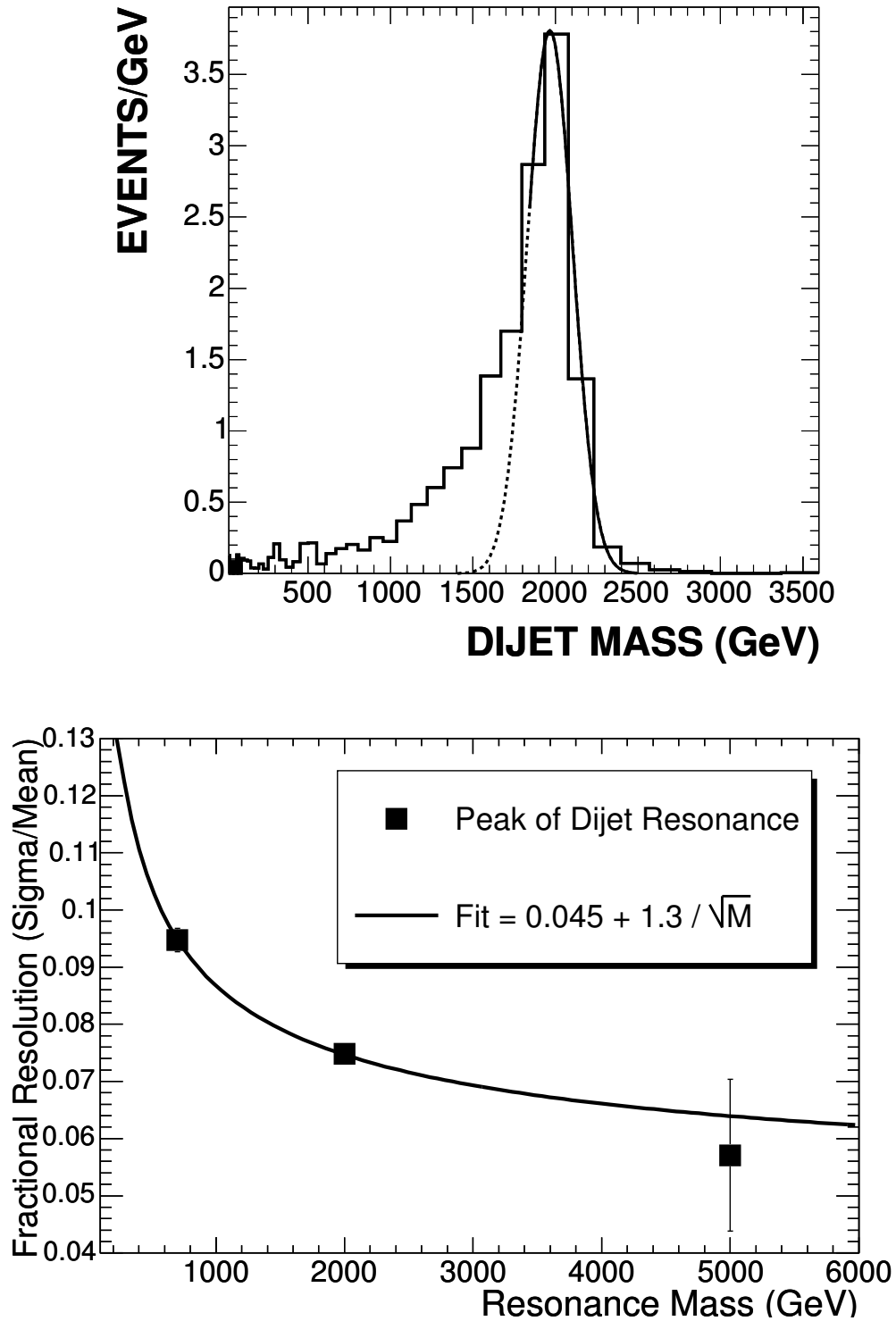


Figure 7: Top) The dijet mass distribution from a 2 TeV Z' (histogram) is fit with a Gaussian (solid curve) on its high mass edge and the Gaussian is extended to lower mass (dashed curve). Bottom) The dijet mass resolution (squares) from Gaussian fits like those above are shown as a function of input Z' mass, M , and fit with a smooth parameterization (solid) of the form $p_0 + p_1/\sqrt{M}$.

4 Search for Resonances

Here we discuss how we plan to search for dijet resonances in the dijet mass distribution with real data. The search is a Bayesian technique based on a binned likelihood [16]. We employ a binned likelihood which uses three distributions in dijet mass m . We form a signal likelihood as a function of signal cross section for any value of dijet resonance mass M . This requires for each dijet mass bin, i :

1. Data: measured number of events, n_i , in data.
2. Background: expected number of events, $N_i(B)$, from background.
3. Signal: number of events, $N_i(S)$, from signal.

The normalization of the signal at this point is arbitrary and $N_i(S)$ could just as well be a probability distribution as a distribution in number of events. We let the size of the signal float by multiplying it by the parameter α to get the mean number of expected events, μ_i , in bin i :

$$\mu_i = \alpha N_i(S) + N_i(B) \quad (1)$$

The probability P_i of observing n_i events when μ_i are predicted is given by Poisson statistics

$$P_i = (\mu_i^{n_i} e^{-\mu_i}) / (n_i!) \quad (2)$$

and the product of P_i over all bins in the mass spectrum is the likelihood function L for seeing the observation given the prediction

$$L = \prod_i P_i. \quad (3)$$

In the absence of systematic uncertainties, this is the likelihood as a function of α for the existence of a dijet resonance of mass M with number of events $\alpha \sum_i N_i(S)$. The number of events is converted into a signal cross section by dividing by the integrated luminosity and accounting for the trigger prescales in each bin. The likelihood in the presence of systematics is determined by convoluting this likelihood with the systematic uncertainty as a function of signal cross section. Then we can look for peaks in the likelihood as a function of signal cross section, and a peak at least 5σ above zero cross section is at the level of a discovery. Otherwise, we can simply use the likelihood distribution to find the signal cross section value that is excluded at 95% confidence. This process is repeated for each value of M , in reasonable steps, to determine the likelihood and any discoveries or exclusions as a function of the resonance mass.

In the actual search we have several options for determining the background. We could use a prediction for the background based on the QCD physics and the expected response of the CMS detector. One way to do this would be to use a complete Monte Carlo approach with a QCD generator and shower Monte Carlo like Pythia followed by the CMS simulation. Another method is to estimate the background from a parton level calculation, perhaps at next-to-leading order or higher, folded with an estimate of the dijet mass resolution in the detector. This method was employed by the D0 experiment at the Tevatron [14]. It has the benefit of being solidly based on a prediction, but has the drawback of needing to understand the possible shape variations of that prediction. Another method is to simply use the data itself to determine the background, by fitting the data to a smooth parameterization, as

was done by the CDF experiment at the Tevatron [17, 8]. It has the benefit of using data in regions away from the resonance to irrefutably determine the background level, but has the drawback that the arbitrary level of flexibility of the parameterization may hide or accentuate resonances at the edge of our sensitivity. Hybrid methods are also possible, for example where the shape of the background is partially or completely determined by QCD and jet resolution, but the normalization of the background is allowed to float until it fits the data. It is not necessary or desirable at this time to decide which method we will choose to determine the QCD background for real data.

The signal distribution is determined by a full simulation of a narrow dijet resonance. This was discussed in section 3. The signal distribution $N_i(S)$ is defined by the resonance simulation in the region $0.3M < m < 1.3M$ and is set to zero everywhere else. This is the mass region where there is reasonable rate from a resonance of mass M . CDF made the same choice of mass range for the resonance distribution in its search [17, 8]. The normalization of the signal floats in the likelihood, so that the likelihood determines what values of signal cross section we either exclude or discover.

5 Sensitivity with Statistical Errors Only

We first consider estimates of our sensitivity with statistical errors only. The sensitivity estimate uses the search technique of the previous section. For these sensitivity estimates we smooth the QCD background to avoid being affected by MC statistics. Fig. 8 shows that the differential cross section for the QCD background is well fit by a simple parameterization of the form

$$\frac{d\sigma}{dm} = \frac{p_0(1 - m/\sqrt{s})^{p_1}}{m^{p_2}} \quad (4)$$

where m is the dijet mass in GeV, $\sqrt{s} = 14000$ GeV is the collision energy, and the parameters found in the fit are $p_0 = 6 \times 10^{14}$ pb/GeV, $p_1 = 8.0$, and $p_2 = 4.8$. We then multiply $d\sigma/dm$ by bin widths and integrated luminosity and divide by prescales to obtain, $N_i(B)$, the number of events in bin i for the background.

We assume two classes of observed data:

1. Data with no signal, where we measure only QCD.
2. Data with a significant signal, where we measure QCD and a 5σ signal.

The signal likelihood distributions from these two classes of observed data are shown in Figure 9 for the case of a 2 TeV/ c^2 narrow resonance. For the likelihood with no signal we set the number of observed events, n_i , equal to the background, $N_i(B)$. Here the signal likelihood peaks at zero cross section, and the 95% CL excluded signal cross section is shown. The likelihood with a 5σ signal is determined in two steps. First we set the number of observed events, n_i , equal to background plus the signal $N_i(S)$ with arbitrary signal rate. We then increase the size of the signal until our likelihood as a function of signal cross section peaks 5σ from zero, where σ is the Gaussian width of the final likelihood distribution. The cross section at which the likelihood peaks is the signal cross section we can discover at 5σ significance. Note that this is a very conservative definition of 5σ discovery. For example, if the background were everywhere exactly zero events, then in order to observe a signal cross section separated by 5σ from zero we would require 25 events.

In Figure 10 we compare the cross section for 95% CL exclusion or 5σ discovery of resonances to the size of the statistical error bars on QCD. We see that the 5σ discovery bumps are clearly well above the statistical error bars. This is expected for a signal at this level of statistical confidence. Conversely, we see that the 95% CL excluded mass bumps peak just above the error bar. This is expected if the observed data agrees with the QCD expectation and we make the statement that the probability of the observed data to have come from a resonance is only 1 chance in 20. We conclude that the likelihood method yields reasonable results.

We evaluate the exclusion and discovery likelihood distributions for each value of the resonance mass from 0.7 TeV to 5.0 TeV in 0.1 TeV steps. For resonance mass values other than 0.7, 2.0 and 5.0 TeV we get the shape of the resonance by interpolation [18]. In Figure 11 we compare our cross section sensitivities with statistical uncertainties only to the lowest order predictions for the resonance cross sections in seven different models. For any resonance model we can read off the expected mass range for either a 95% CL exclusion or a 5σ significance discovery. The mass sensitivity is tabulated in table 3. Mass sensitivities above 5 TeV were determined by linear extrapolation of the 95% CL and 5σ discovery cross sections in Figure 11. For an integrated luminosity of 10 fb^{-1} , with statistical uncertainties only, CMS can discover with 5σ significance an excited quark of mass as high as 5.0 TeV. This is about the same as a previous estimate of excited quark discovery mass reach at the LHC [19], which was 5.3 TeV for the same integrated luminosity and level of significance.

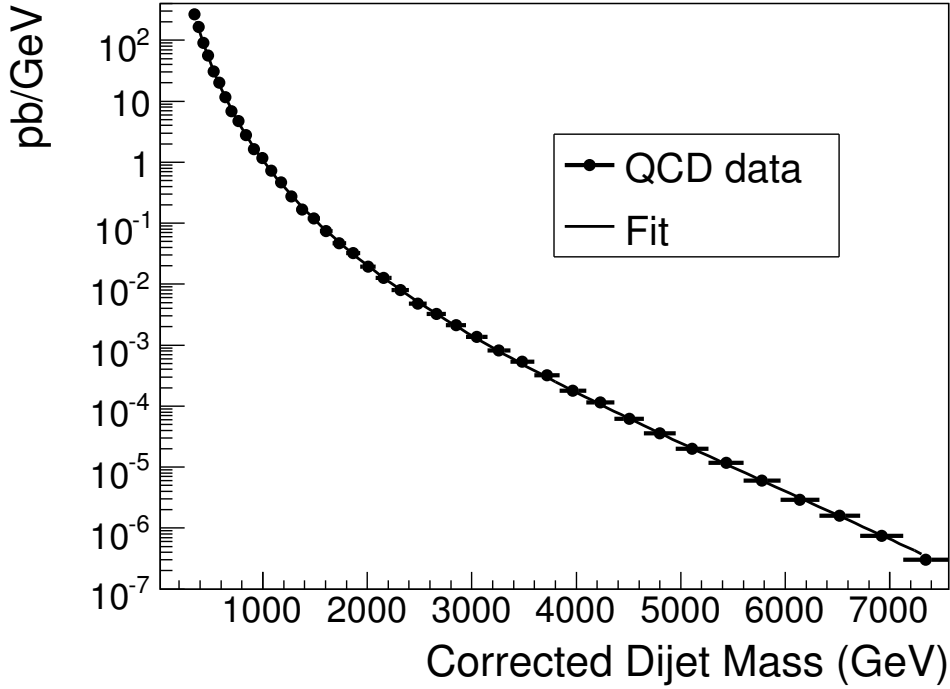


Figure 8: The full CMS simulation of the QCD differential cross section vs. dijet mass (points) is fit to a smooth parameterization (curve).

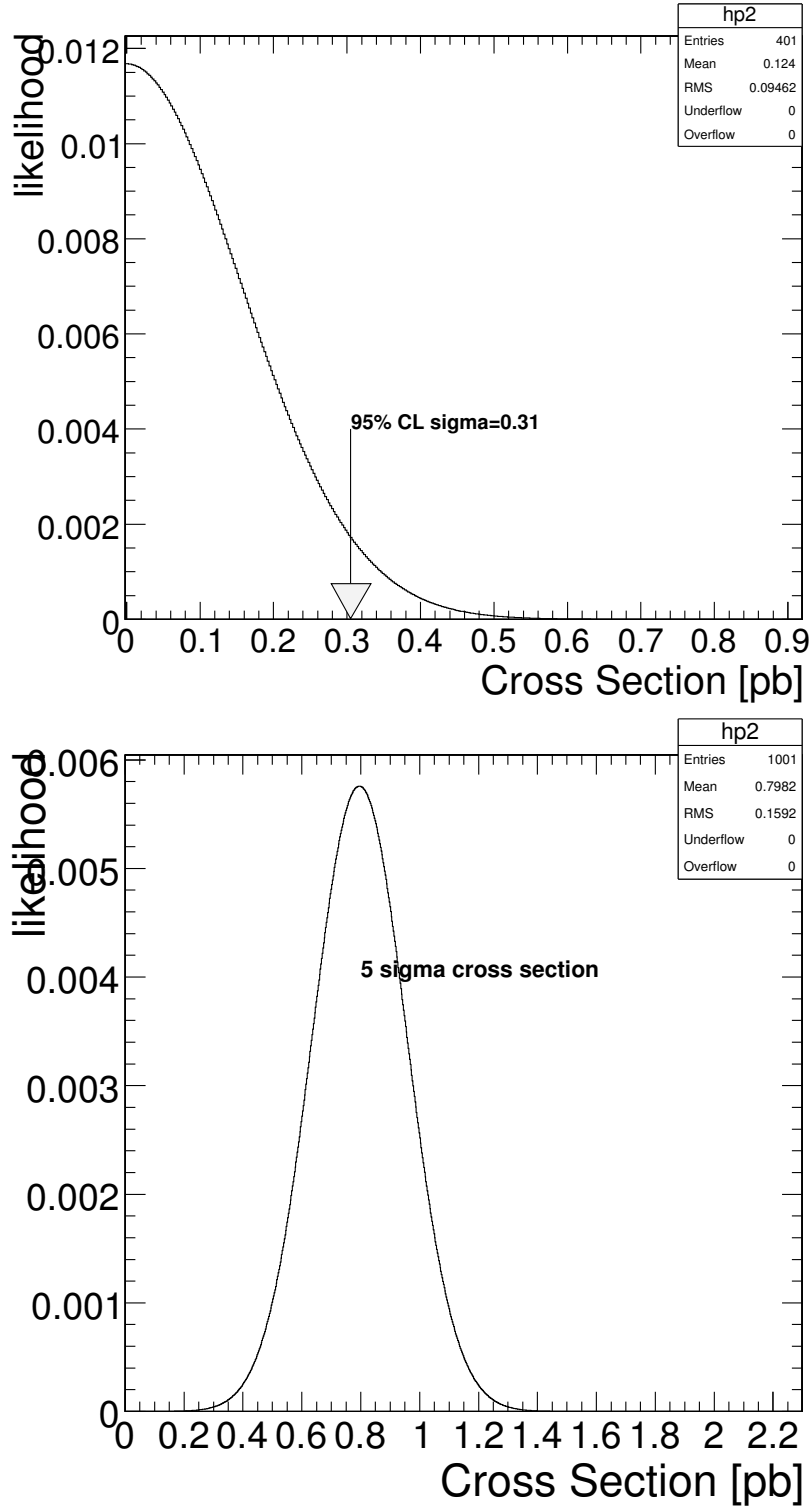


Figure 9: Likelihoods with statistical uncertainties only for observing a narrow dijet resonance of mass $2 \text{ TeV}/c^2$ in a 1 fb^{-1} data sample that contains only QCD background (top) and a data sample that also contains a resonance with a significance of 5σ (bottom).

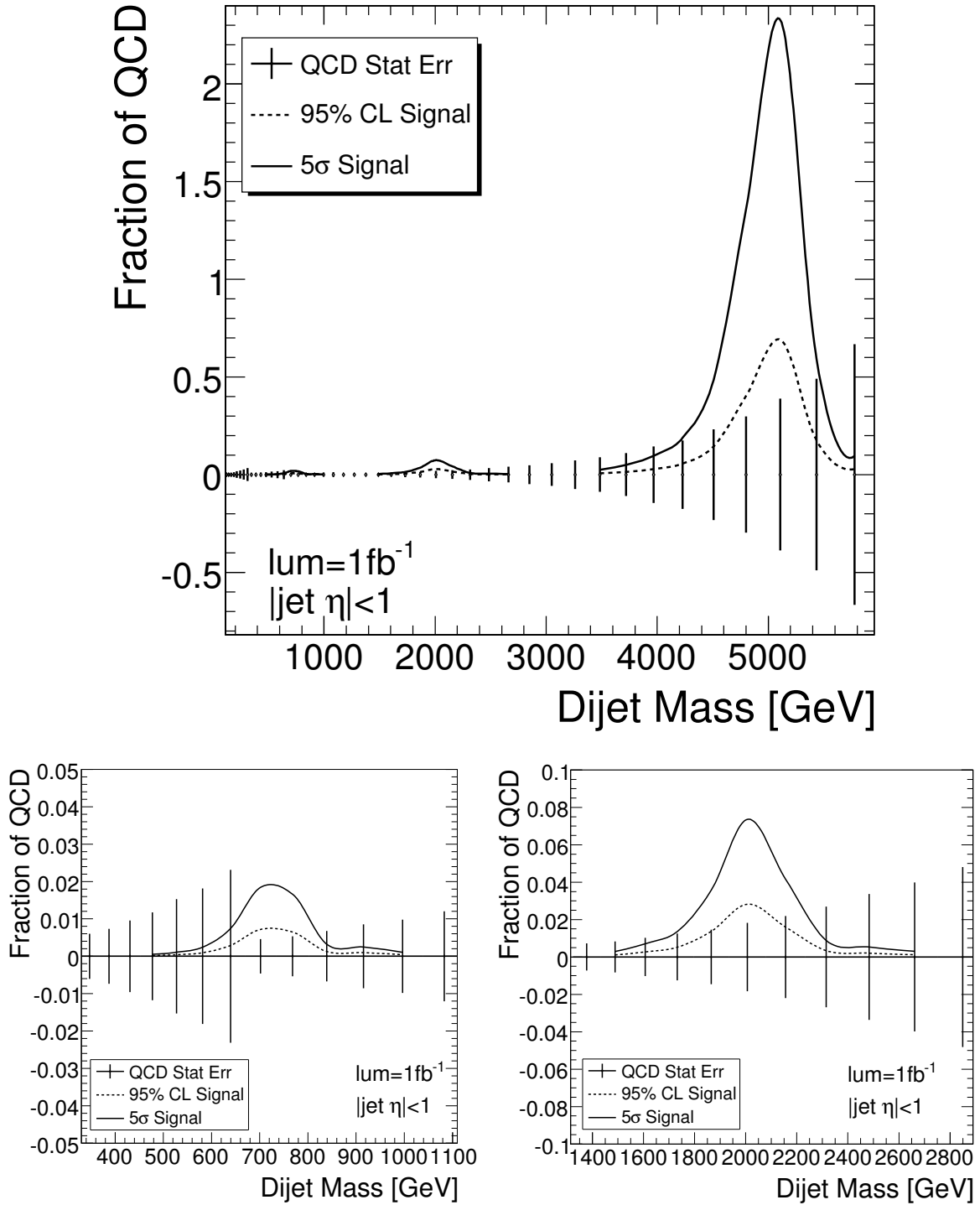


Figure 10: Top) The cross section of resonance signals at 0.7, 2.0, and 5.0 TeV that could be excluded at 95% CL (dashed) or discovered with 5 σ significance (solid) including statistical uncertainties only, is shown as a fraction of the QCD background and compared to the statistical errors on the QCD background for a sample of size 1 fb^{-1} . Bottom Left) Zoomed view for a 0.7 TeV resonance. Bottom Right) Zoomed view for a 2.0 TeV resonance.

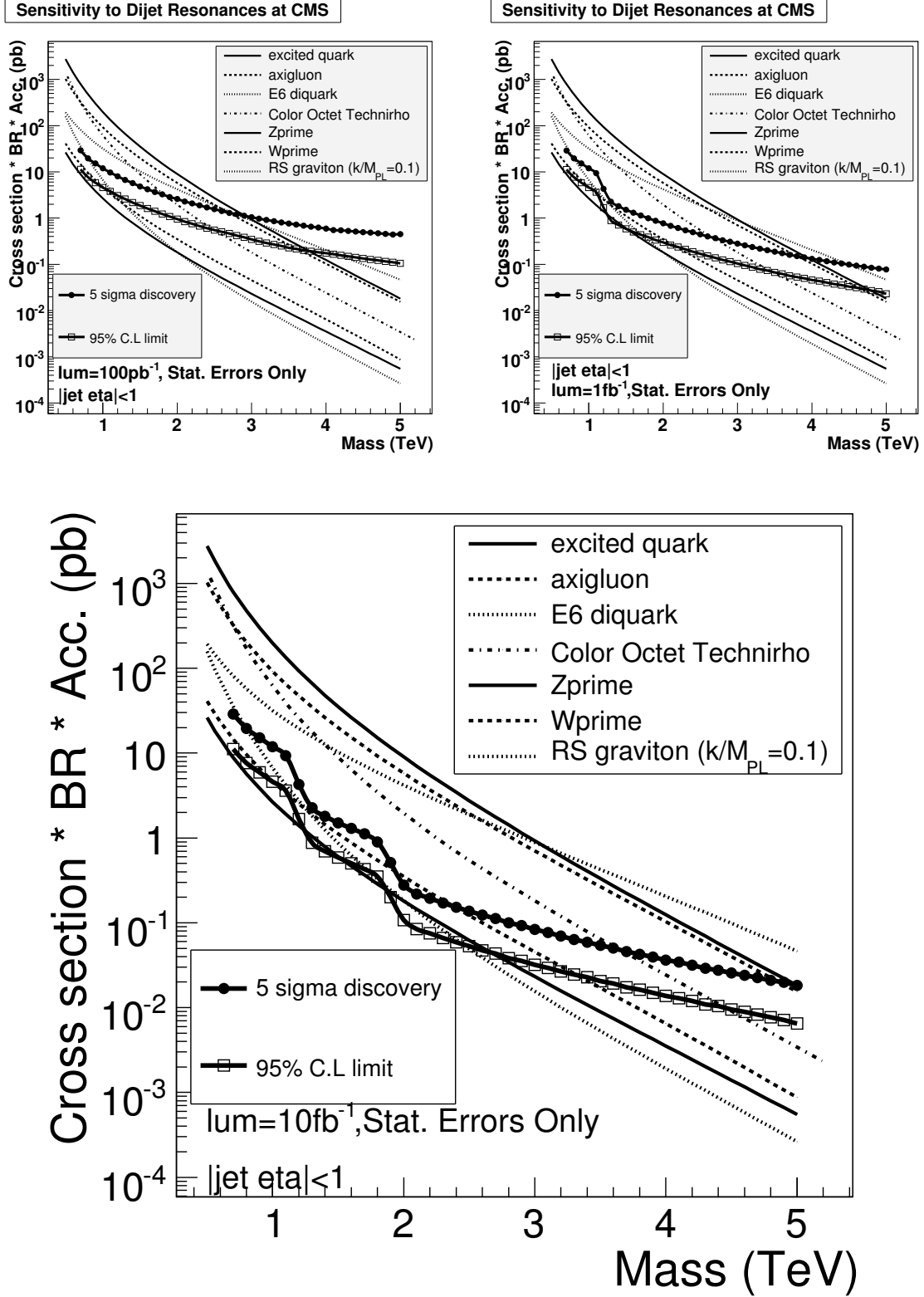


Figure 11: Dijet resonance sensitivity for 100 pb^{-1} (top left), 1 fb^{-1} (top right), and 10 fb^{-1} (bottom). The cross section of a resonance signal that could be discovered with 5σ significance (black dots) or excluded at 95% CL (open boxes) is compared to the cross section for various resonance models. These sensitivities contain STATISTICAL UNCERTAINTIES ONLY.

Resonance Model	95% CL Excluded Mass (TeV/ c^2)			5 σ Discovered Mass (TeV/ c^2)		
	100 pb $^{-1}$	1 fb $^{-1}$	10 fb $^{-1}$	100 pb $^{-1}$	1 fb $^{-1}$	10 fb $^{-1}$
Excited Quark	0.7 - 3.8	0.7 - 4.8	0.7 - 5.8	0.7 - 2.9	0.7 - 3.9	0.7 - 5.0
Axigluon or Coloron	0.7 - 3.6	0.7 - 4.6	0.7 - 5.6	0.7 - 2.6	0.7 - 3.8	0.7 - 4.8
E_6 diquark	0.7 - 4.1	0.7 - 5.6	0.7 - 7.0	0.7 - 2.8	0.7 - 4.5	0.7 - 6.0
Color Octet Technirho	0.7 - 2.4	0.7 - 3.4	0.7 - 4.5	0.7 - 1.8	0.7 - 2.6	0.7 - 3.6
Randall-Sundrum Graviton	0.7 - 1.1	0.7 - 1.7	0.7 - 1.7 1.9 - 2.4	0.7 - 0.8	0.7 - 0.8	0.7 - 0.8
W'	0.7 - 1.0	0.7 - 1.0 1.2 - 2.1	0.7 - 1.0 1.2 - 3.4	N/A	N/A	2.0 - 2.3
Z'	N/A	1.2 - 1.5	1.3 - 1.5 1.9 - 2.6	N/A	N/A	N/A

Table 3: Sensitivity to dijet resonances with 100 pb $^{-1}$, 1 fb $^{-1}$, and 10 fb $^{-1}$. For each resonance model, we show the range of masses we expect to be able to exclude at a confidence level of 95% or greater, and the range of masses we expect to be able to discover with a significance of 5 σ or greater. All estimates are with STATISTICAL UNCERTAINTIES ONLY.

6 Systematic Uncertainties

The systematic uncertainties in searching for dijet resonances are dominated by the uncertainty in the background. Even uncertainties on the shape of the resonance are only significant if there is a background underneath the resonance. The QCD dijet background is large and steeply falling with dijet mass, and this will affect almost all of the systematics we examine. For each of our sources of systematic uncertainty we determine the 1σ change in the signal cross section that we can exclude or discover. We combine these 1σ changes in quadrature to determine the total systematic uncertainty. We then use this total systematic in the next section to convolute our statistical likelihoods and find estimates of the exclusion and discovery cross sections in the presence of all systematics.

In Fig. 12 we summarize the individual systematic uncertainties and the total systematic uncertainty in our signal sensitivity for 10 fb $^{-1}$ expressed as a fraction of the signal cross section. While it is expressed as a fraction, it is important to realize that the way one gets the actual systematic for exclusion or discovery is to multiply this fraction by the values of the exclusion or discovery cross section limits in Fig 11, which gives an absolute cross section uncertainty which is then invariant as a function of signal size. This is important to appreciate, since if one mistakenly views this as an uncertainty on the size of any signal cross section, one would conclude that it was impossible to have a 5 σ discovery regardless of signal size. We know that a 5 σ discovery is possible if one can have an arbitrarily large signal in a localized region of dijet mass, and in the next section we will estimate how large the signal cross section must be for it to be 5 σ away from zero. In the remainder of this section we discuss the individual systematics that contribute to Fig. 12.

6.1 Jet Energy Scale

CMS has concluded that an uncertainty on the jet energy scale of $\pm 5\%$ is achievable [10, 20]. The resulting systematic uncertainty on the cross section of the QCD background shown in Fig 5 varies from about 30% at a dijet mass of 0.7 TeV to 60% at a dijet mass of 5 TeV. We

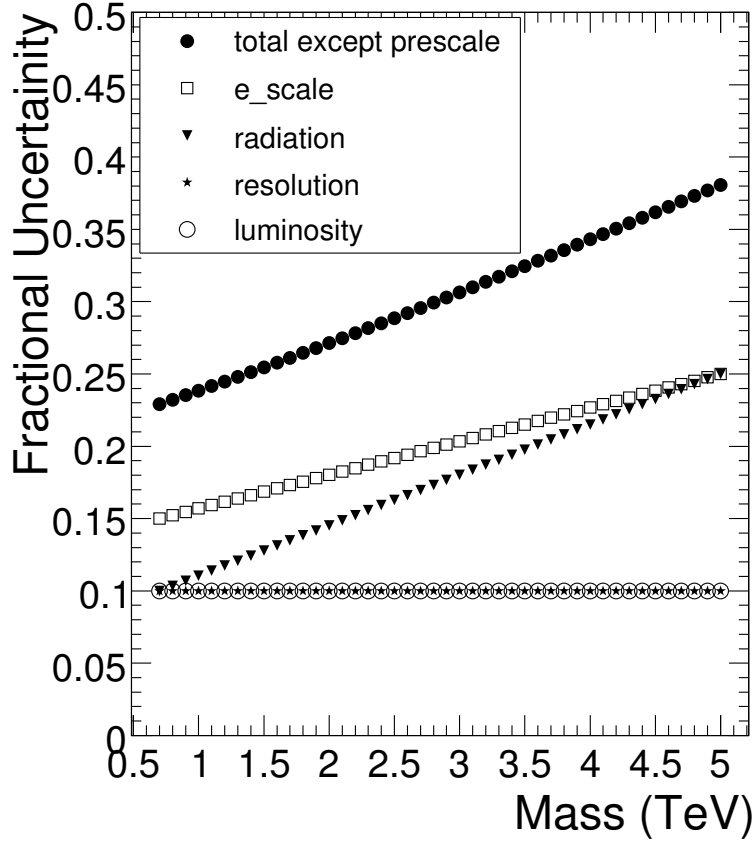


Figure 12: Fractional systematic uncertainties on signal cross section sensitivity. The uncertainties from smallest to largest are from luminosity (open circles), dijet mass resolution (stars), low mass tail of resonance including radiation (triangles), jet energy scale effect on QCD background (open boxes), and the total from these systematics added in quadrature (black dots). There is also a trigger prescale systematic from jet energy uncertainties which occurs for mass values of 0.7, 1.2, 1.3, 1.9, 2.0 and 2.1 TeV and is discussed in the text but not included in this plot.

increased the QCD background by this systematic and computed new values for the cross section limits and discovery values for 10 fb^{-1} . The signal cross section increased by an amount which varied from about 15% at a resonance mass of 0.7 TeV to 25% at a resonance mass of 5 TeV, as shown in Fig. 12. As expected, the increase in signal cross section was just the square root of the increase in background, since our sensitivity was being held constant at 95% CL and at 5σ , and the sensitivity is proportional to $\text{signal}/\sqrt{\text{background}}$ where the background is large.

The jet energy scale systematic as a function of resonance mass can also be found from the cross section sensitivity curves in Fig. 11, by starting at any mass of interest and moving to a point on the curve at 5% lower mass. This is essentially moving the signal down to a 5% lower mass value while keeping the background fixed as a function of mass, which is equivalent to raising the background underneath a fixed signal. For the 10 fb^{-1} curve this gave the same result as shown in Fig. 12 to within a few percent, except for the regions

where the trigger prescale changes, which we discuss in the next section. We also repeated this check with the 1 fb^{-1} and the 100 pb^{-1} samples, and the systematic change was always equal to or lower than the shift we observed in the 10 fb^{-1} sample, except of course near the trigger prescale changes. These lower systematics shifts are expected for the 1 fb^{-1} and the 100 pb^{-1} samples, because the background number of events are smaller and the sensitivity is more accurately given by $\text{signal}/\sqrt{\text{signal} + \text{background}}$. To be conservative and keep things simple we assigned the jet energy systematic shown in Fig. 12 to all three integrated luminosity samples.

6.2 Jet Energy Scale and Trigger Prescales

If a resonance is contained within an unprescaled trigger, or a low prescaled trigger, CMS will be more sensitive to the resonance than if the prescales are larger. There is thus a signal systematic, due to our uncertainty in the resonance position in dijet mass, at those resonance mass values close to the dijet mass threshold where the prescale changes. This systematic only has the effect of delaying the benefit of the lower prescale until a mass value where most of the resonance is contained within that lower prescale. It is essentially an edge effect of our measurement region. An illustration of this edge is the comparison of a 0.7 TeV dijet resonance to the error in the QCD background in the bottom left plot of Figure 10. The jet energy scale uncertainty of 5% has its largest effect at dijet mass values just above where the trigger prescale has changed. The prescale changes at a dijet mass value of 0.67 TeV for the 100 pb^{-1} sample, at dijet mass values of 0.67 and 1.13 TeV for the 1 fb^{-1} sample, and at dijet mass values of 0.67, 1.13 and 1.80 TeV for the 10 fb^{-1} sample. Just below these thresholds the number of both signal and background events drops precipitously. As can be seen in Fig. 11 our statistical sensitivity to a resonance is significantly reduced just below these thresholds. Just above these thresholds reducing the dijet mass by its 5% uncertainty greatly increases the cross section required to observe a resonance, and the cross section we can exclude. The amount of this uncertainty, obtained by sliding the resonances to lower mass values and seeing what change results is listed in table. 4. The systematic at 1.9, 2.0 and 2.1 TeV are only for 10 fb^{-1} , those at 1.2 and 1.3 TeV are only for 1 fb^{-1} and 10 fb^{-1} , and the one at 0.7 TeV is for 100 pb^{-1} , 1 fb^{-1} and 10 fb^{-1} .

Mass (TeV)	e-scale/prescale Systematic	Samples Affected
0.7	100%	100 pb^{-1} , 1 fb^{-1} , 10 fb^{-1}
1.2	70%	1 fb^{-1} , 10 fb^{-1}
1.3	60%	1 fb^{-1} , 10 fb^{-1}
1.9	70%	10 fb^{-1}
2.0	130%	10 fb^{-1}
2.1	30%	10 fb^{-1}

Table 4: e-scale/prescale systematic uncertainty. For the resonance masses where there is this systematic uncertainty, we list the value of the systematic uncertainty, and the samples to which the systematic uncertainty applies.

6.3 Jet Energy Resolution

Here we discuss the uncertainty on the dijet resonance signal from uncertainties in jet energy resolution. We consider the systematic on the shape of the resonance due to calorimeter re-

sponse uncertainties. The full effect of the calorimeter on dijet mass resonances line shape is shown in Fig. 13. The true dijet mass distribution from a resonance, using GenJets reconstructed at the particle level before they interact in the calorimeter, is compared with our measured and corrected dijet mass distribution using RecJets. The GenJets show only slightly better resolution than the RecJets, because at these high dijet masses the calorimeter resolution is quite good.

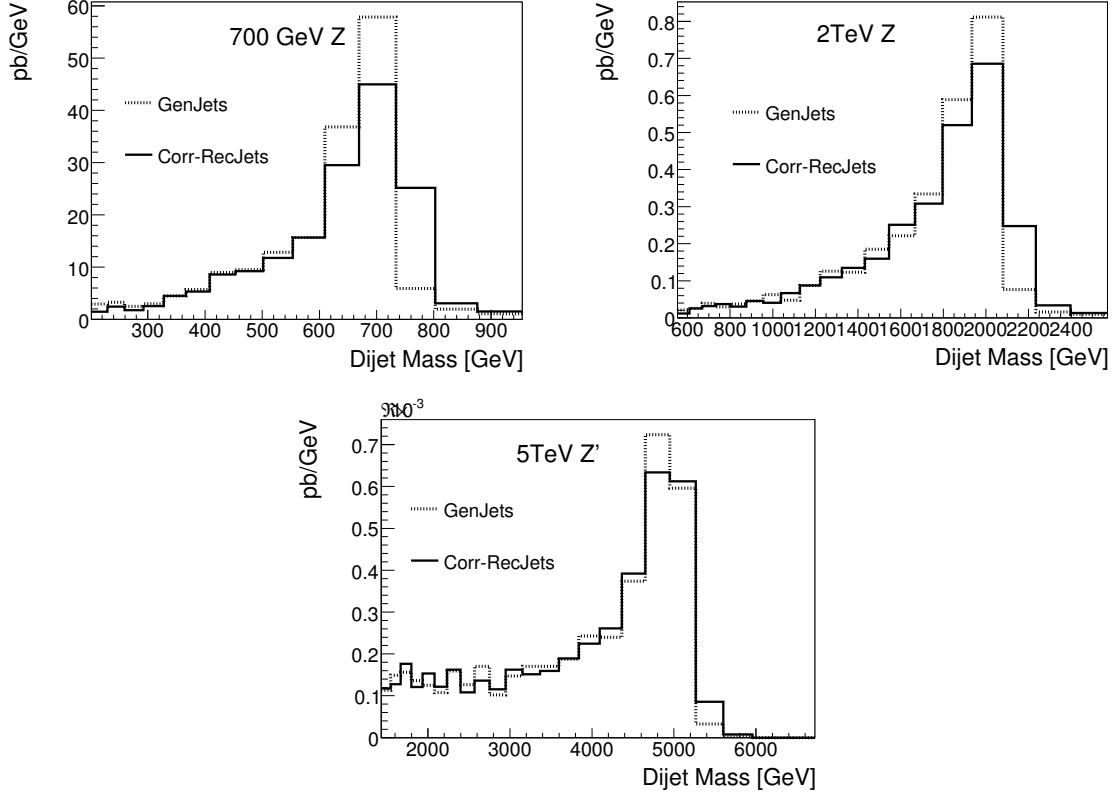


Figure 13: Dijet resonances of mass 0.7 TeV (Top Left Plot), 2.0 TeV (Top Right Plot) and 5.0 TeV (Bottom Plot) from GenJets reconstructed from MC particles (dotted) is compared to resonances reconstructed using the standard measured and corrected dijets (solid).

We used the shape of the dijet resonances from GenJets to compute new values for the cross section limits and discovery values for 10 fb^{-1} . The resulting exclusion and discovery cross sections were reduced by only about 5% when using GenJets for all masses except near the prescale thresholds, where the cross section increased by about 50%. The increase at the prescale thresholds was due to a small mass shift between dijet masses made with GenJets and those made with RecJets, which varied from about 2% at 0.7 TeV to about 0.6% at 5 TeV. The mass shift also has an effect at all masses, producing an increase in the exclusion and discovery cross sections of about 5%. The first 5% change we measured therefore comes from two effects, one from improved resolution which lowers the cross section limits by 10% , and the other from the small mass shift which raised the cross section limits by 5%. Thus after disentangling the two effects, we find that the calorimeter broadening of the dijet mass peak, without allowing it shift the mass at all, changes our sensitivity by 10%. We take this full affect of the calorimeter on the resolution as a systematic uncertainty on the resolution,

which is most likely an overestimate. We use the 10% resolution uncertainty shown in Fig. 12 for all luminosities.

6.4 Radiation and Resonance Low Mass Tail

Here we discuss the uncertainty on the dijet resonance signal from uncertainties in the long tail to low mass. Most of this tail comes from energy lost from the jet cone by gluon radiation off a final state parton. Radiation may depend on the type of resonance, including for example its color multiplicity and whether it decays to quarks or gluons, which will affect our generic model of the resonance shape. Also, at very high resonance mass some of the tail is also due to the huge parton distributions at very low dijet mass multiplying the Breit-Wigner tail of the resonance. This is demonstrated in Figure 14 where we see a long low mass tail at the generator level for a 5 TeV Z' resonance but do not see one for a 2 TeV Z' resonance, and this then affects both the particle level and calorimeter level jets in Figure 13. The size of this effect depends on the width of the narrow resonance and the kind of partons in the initial state, and again somewhat affects the assumption that all narrow resonances look the same.

We estimate the size of all these uncertainties in the long tail to low mass by narrowing the range of dijet mass we consider for each resonance. For a dijet resonance of mass M the default range in dijet mass, m , used by the analysis is $0.3M < m < 1.3M$ which incorporates both the core of the resonance and the long tail to low mass. We remove most of the long tail to low mass by using the symmetric dijet mass range $0.7M < m < 1.3M$ instead. In both cases the total cross section of the resonance is forced to be the same, so that for the default case the resonance cross section is spread out toward low dijet mass, while for the symmetric case the same total resonance cross section is concentrated in dijet mass around the resonance mass M . Clearly the symmetric case sees less background underneath the smaller mass window and provides more sensitivity to dijet resonances, and the magnitude of this change in sensitivity tells us the magnitude of the effect of the long tail to low mass. We used the mass window $0.7M < m < 1.3M$ to compute new values for the cross section limits and discovery values for 10 fb^{-1} , which decreased by about the fractional values shown in Fig. 12. This systematic increases from 10% at $M = 0.7 \text{ TeV}$ to 25% at $M = 5.0 \text{ TeV}$. We use this systematic for all luminosities. This is conservative because at 1 fb^{-1} and 100 pb^{-1} we expect a smaller systematic, since the background under our window is reduced, and the sensitivity to changing the window size is therefore also reduced.

6.5 Luminosity

To the best of our knowledge there has been no CMS study of what uncertainty we can expect in the measurement of the LHC luminosity. From the prior experience of the Tevatron we expect the uncertainty in the luminosity to be around 10%. The uncertainty in the luminosity directly affects any translation of a discovered or excluded number of events into a corresponding cross section. Thus, while it does not strictly affect the discovery or exclusion, since these can be thought of as number of events values equally as luminosities. However, it does affect the resulting cross sections, which we seek to estimate for our sensitivities and comparing with models, so we include it in our total systematics.

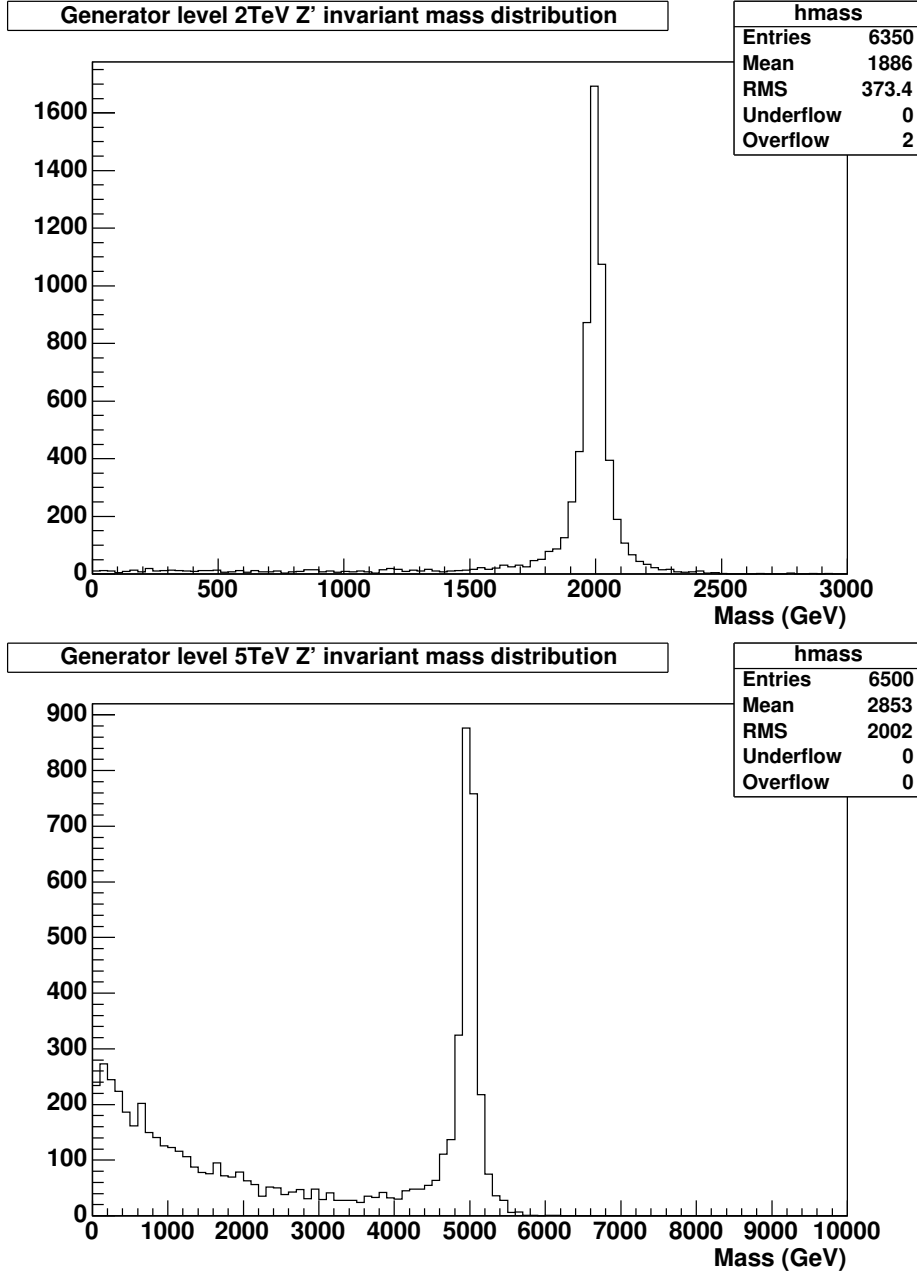


Figure 14: Z' resonances at the generator level for pole mass 2.0 TeV (Top Plot) and 5.0 TeV (Bottom Plot). The horizontal axis is the output resonance mass, $\sqrt{\hat{s}}$, resulting from the specified pole mass.

7 Sensitivity including Systematic Uncertainties

Here we include the total systematic uncertainty of the previous section in our likelihoods to estimate the exclusion and discovery cross sections with systematic uncertainties. We start with the likelihood functions with statistical errors only discussed in section 5. We then convolute those likelihood functions with Gaussian systematic uncertainties. For the exclusion (discovery) likelihoods the width of the Gaussian systematic at any value of resonance mass is given by the exclusion (discovery) cross section in Fig. 11 times its fractional uncertainty given in Fig. 12. This is all that needs to be done for the exclusion likelihoods, and we get new 95% CL exclusion cross sections that include systematics. For the discovery likelihoods, the previously 5σ discovery cross section with statistical errors only have now been degraded with systematics and are significantly less than 5σ . We increase the cross section of the resonance until the discovery likelihoods with systematics are once again 5σ away from zero. The resulting exclusion and discovery likelihoods from this procedure are shown in Fig. 15 for a 2 TeV resonance and 1 fb^{-1} of data.

Systematic uncertainties have a much greater effect on the discovery likelihoods than the exclusion likelihoods. This is simply because the measurement uncertainty of a signal cross section is dominated by poor statistics when there is no signal, and the measurement uncertainty is dominated by systematics when there is so large a signal that we can make a 5σ statistical discovery. In Figure 15 we see for this particular value of resonance mass and integrated luminosity that systematics increased by 15% the cross section we can exclude at 95% confidence level and increased by 70% the cross section we can discover at 5σ .

Since the discovery likelihoods include sizable systematic uncertainties, conservatively estimated, they need to be interpreted cautiously. They are not precise statements of likelihood. They are estimates of how large the signal cross section might have to be in order to make a 5σ discovery. Clearly we do not believe that our systematic uncertainties have perfectly Gaussian shape all the way out to 5σ . For conservative estimates of our sensitivity, this procedure is quite adequate, but requires us to be vigilant that our results make physical sense.

For each integrated luminosity we have convoluted all our exclusion likelihoods with Gaussian systematic uncertainties, found new exclusion cross sections, and compared them with the old values with statistical uncertainties only. Except for the mass regions just above the prescale thresholds, the value of the 95% CL excluded cross section increased by 10% at low resonance mass and 25% at the highest resonance mass, independent of integrated luminosity. These changes can be simply understood. Given that a 95% CL is about 1.6σ on a one sided Gaussian, the effective width of the exclusion likelihoods in units of their 95% CL cross section point is just $1/1.6=60\%$. If we take this width and add it in quadrature with the systematic uncertainty in Figure 12 we get a changes in the width of the exclusion likelihood that vary from roughly 10% at low resonance mass to 20% at the highest resonance mass. The Gaussian expected change at the highest resonance mass is slightly below what we found because of Poisson statistics. Just above the prescale thresholds the increase in the excluded cross sections is much larger, ranging from as little as 30% to as much as 200%.

For each integrated luminosity we have convoluted all our discovery likelihoods with Gaussian systematic uncertainties, found new discovery cross sections, and compared them with the old values with statistical uncertainties only. Except for the mass regions just above the prescale thresholds, the value of the 5σ discovery cross section increased by 50% at low resonance mass and 110% at the highest resonance mass, independent of integrated luminosity. These changes can also be simply understood. The width of the 5σ likelihood is by defini-

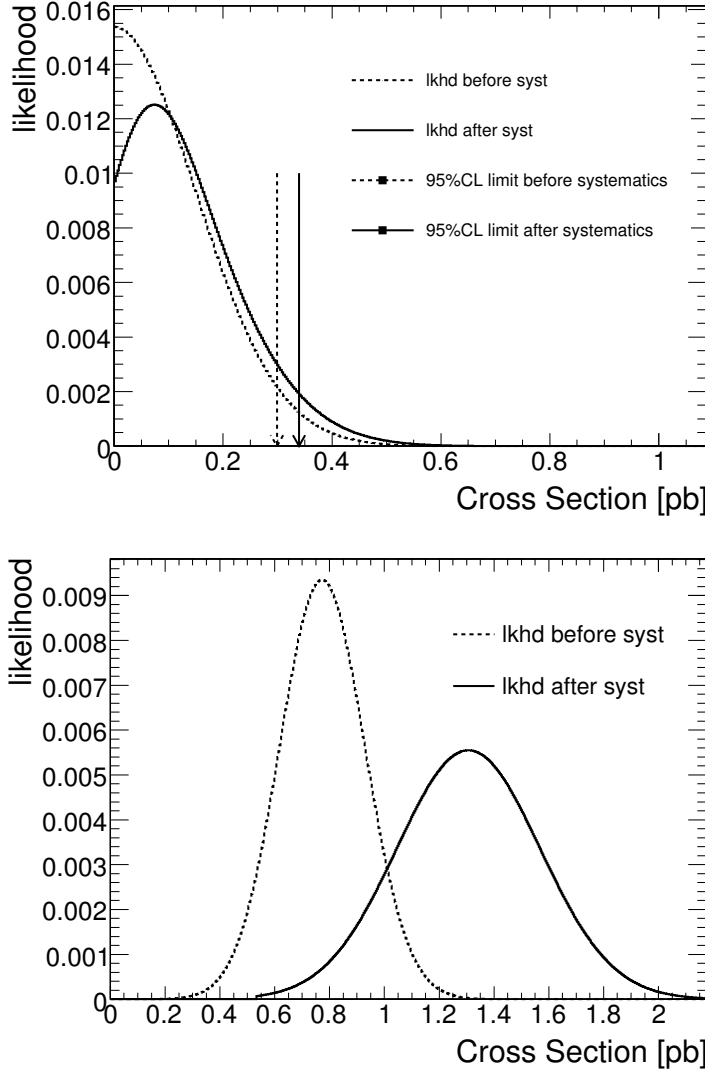


Figure 15: Likelihoods for observing a narrow dijet resonance of mass $2 \text{ TeV}/c^2$ in a 1 fb^{-1} data sample that contains only QCD background (top) and a data sample that also contains a resonance with a significance of 5σ (bottom). The likelihoods with statistical uncertainties only (dashed curve) is compared to the likelihood with both statistical and systematic uncertainties (solid curve).

tion 20%. If we take this width and add it in quadrature with the systematic uncertainty in Figure 12 we get a new width for the discovery likelihood that ranges from 30% at low resonance mass to 42% at the highest resonance mass. The new resonance cross section that restores a 5σ effect is the one that gives a 20% total width, which requires the cross section to increase by $30/20 - 1 = 50\%$ at low mass and by $42/20 - 1 = 110\%$ at the highest resonance mass. There is nothing mysterious about the convolutions and the resulting likelihoods.

For resonances with masses just above the dijet mass values where the prescale changes, large systematic uncertainties increased the discovery cross section by between 100% and 700%. This change is again simply understood by the mathematics of the method. However,

for resonance mass values of 1.2, 1.9 and 2.0 TeV the changes were larger than physically allowable. For the 10 fb^{-1} sample, where the unprescaled trigger begins at 1.8 TeV, we know that the discovery cross section for 1.9 TeV and 2.0 TeV resonance masses region cannot be any worse than the discovery cross section for the 1 fb^{-1} sample. While it is true that we are uncertainty whether the signal got prescaled, by falling beneath the prescale threshold, even if it all the signal got prescaled it would still have exactly the same rate as the 1 fb^{-1} sample, and therefore this cross section is a physical upper limit on the discovery cross section for the 10 fb^{-1} sample. A similar statement is also true for the 1.2 TeV resonance mass, and there the check involves all three samples. We know that the exceeding of the physically possible values is due to assuming the distribution of the very large e-scale/prescale systematic uncertainty is Gaussian. Instead it clearly has a distribution that can only go out to a certain point, and then must stop. We explicitly implement this stopping point with the known physical constraint from the lower integrated luminosity sample. We put a physical constraint on the 5σ discovery cross section for the 1.9 and 2.0 TeV resonances in the 10 fb^{-1} sample, and on 1.2 TeV mass resonances in the 10 fb^{-1} and 1 fb^{-1} sample, which limited their discovery cross section to that in the previous sample. Thus the affect of the e-scale/prescale systematic is effectively to delay the utility of any new prescaled trigger until dijet mass values that completely contain the core of the dijet resonance.

In Table 5 we list the cross section sensitivities with both statistical and systematic uncertainties. In Fig. 16 we compare these sensitivities to the lowest order predictions for the resonance cross sections in seven different models. For any resonance model we can read off the expected mass range for either a 95% CL exclusion or a 5σ significance discovery. The mass sensitivity is tabulated in table 6. Since now we have included systematics and are quoting conservative values, mass sensitivities above 5 TeV were determined by using the excluded or discovered cross section values at 5 TeV (assumes the cross section levels out). Linear extrapolation of the cross section would instead give a slightly larger mass sensitivity at 95% CL of 6.8 TeV for E_6 diquarks, 5.6 TeV for excited quarks, and 5.5 TeV for axigluons or colorons.

Our lower bound on mass sensitivity for a 95% CL exclusion in table 6 connects with the Tevatron exclusions in table 1 for excited quarks, axigluons, colorons and W' . However, it does not connect with the Tevatron exclusions of E_6 diquarks, color octet technirhos or Z' , and there are no published searches for Randall-Sundrum gravitons decaying to dijets from the Tevatron. Our estimates of sensitivity began at a resonance mass of 0.7 TeV, just within our first unprescaled trigger. That is why 0.7 TeV is frequently the lower bound on expected exclusion or discovery quoted in table 6. It is therefore likely that CMS has some sensitivity to even lower mass resonances, but this has not yet been estimated for resonance masses beneath 0.7 TeV. From the cross sections in Figure 16 we expect that if the analysis were extended to lower mass our 95% CL sensitivity should connect with the Tevatron exclusions for the case of E_6 diquarks and color octet technirhos as well. If more sensitivity than this is required at low resonance mass, alternative trigger strategies discussed at the end of section 2.2 could always be employed.

M TeV/ c^2	95% CL Exclusion (pb)			5 σ Discovery (pb)		
	100 pb $^{-1}$	1 fb $^{-1}$	10 fb $^{-1}$	100 pb $^{-1}$	1 fb $^{-1}$	10 fb $^{-1}$
0.7	26	26	26	150	150	150
0.8	8.4	8.4	8.4	30	30	30
0.9	6.5	6.5	6.5	23	23	23
1.0	5.1	5.1	5.1	19	19	19
1.1	4.2	4.0	4.0	15	15	15
1.2	3.4	3.1	3.1	13	13	13
1.3	2.9	1.5	1.5	11	7.7	7.7
1.4	2.4	0.79	0.77	9.2	2.9	2.9
1.5	2.1	0.66	0.65	7.9	2.5	2.4
1.6	1.8	0.56	0.56	6.9	2.1	2.1
1.7	1.6	0.49	0.49	6.1	1.9	1.8
1.8	1.4	0.44	0.40	5.4	1.7	1.5
1.9	1.2	0.38	0.37	4.8	1.5	1.5
2.0	1.1	0.34	0.32	4.4	1.3	1.3
2.1	0.95	0.30	0.11	3.9	1.2	0.50
2.2	0.86	0.27	0.085	3.6	1.1	0.33
2.3	0.77	0.24	0.076	3.3	0.95	0.30
2.4	0.70	0.22	0.068	3.0	0.86	0.27
2.5	0.64	0.19	0.061	2.8	0.78	0.24
2.6	0.58	0.18	0.055	2.5	0.71	0.22
2.7	0.54	0.16	0.050	2.4	0.66	0.20
2.8	0.49	0.14	0.045	2.2	0.60	0.18
2.9	0.45	0.13	0.042	2.1	0.56	0.17
3.0	0.41	0.12	0.038	1.9	0.51	0.15
3.1	0.37	0.11	0.034	1.8	0.48	0.14
3.2	0.34	0.10	0.032	1.7	0.44	0.13
3.3	0.31	0.093	0.029	1.6	0.41	0.12
3.4	0.29	0.087	0.027	1.5	0.39	0.11
3.5	0.27	0.080	0.025	1.5	0.36	0.10
3.6	0.25	0.074	0.023	1.4	0.34	0.10
3.7	0.24	0.068	0.021	1.3	0.31	0.089
3.8	0.23	0.064	0.020	1.3	0.30	0.084
3.9	0.22	0.060	0.018	1.2	0.28	0.078
4.0	0.21	0.055	0.017	1.2	0.26	0.073
4.1	0.20	0.053	0.016	1.1	0.25	0.069
4.2	0.19	0.049	0.015	1.1	0.24	0.064
4.3	0.18	0.046	0.013	1.1	0.23	0.060
4.4	0.17	0.044	0.013	1.1	0.22	0.057
4.5	0.16	0.041	0.012	1.0	0.21	0.053
4.6	0.16	0.039	0.011	1.0	0.20	0.050
4.7	0.15	0.036	0.010	0.99	0.19	0.048
4.8	0.14	0.034	0.010	0.98	0.18	0.045
4.9	0.14	0.032	0.0090	0.96	0.17	0.043
5.0	0.13	0.030	0.0081	0.98	0.17	0.040

Table 5: Cross section sensitivity to dijet resonances with 100 pb $^{-1}$, 1 fb $^{-1}$, and 10 fb $^{-1}$. For each mass of narrow dijet resonance considered we list the cross section that we expect to be able to exclude at 95% CL and the cross section that we expect to be able to discover with 5 σ significance.

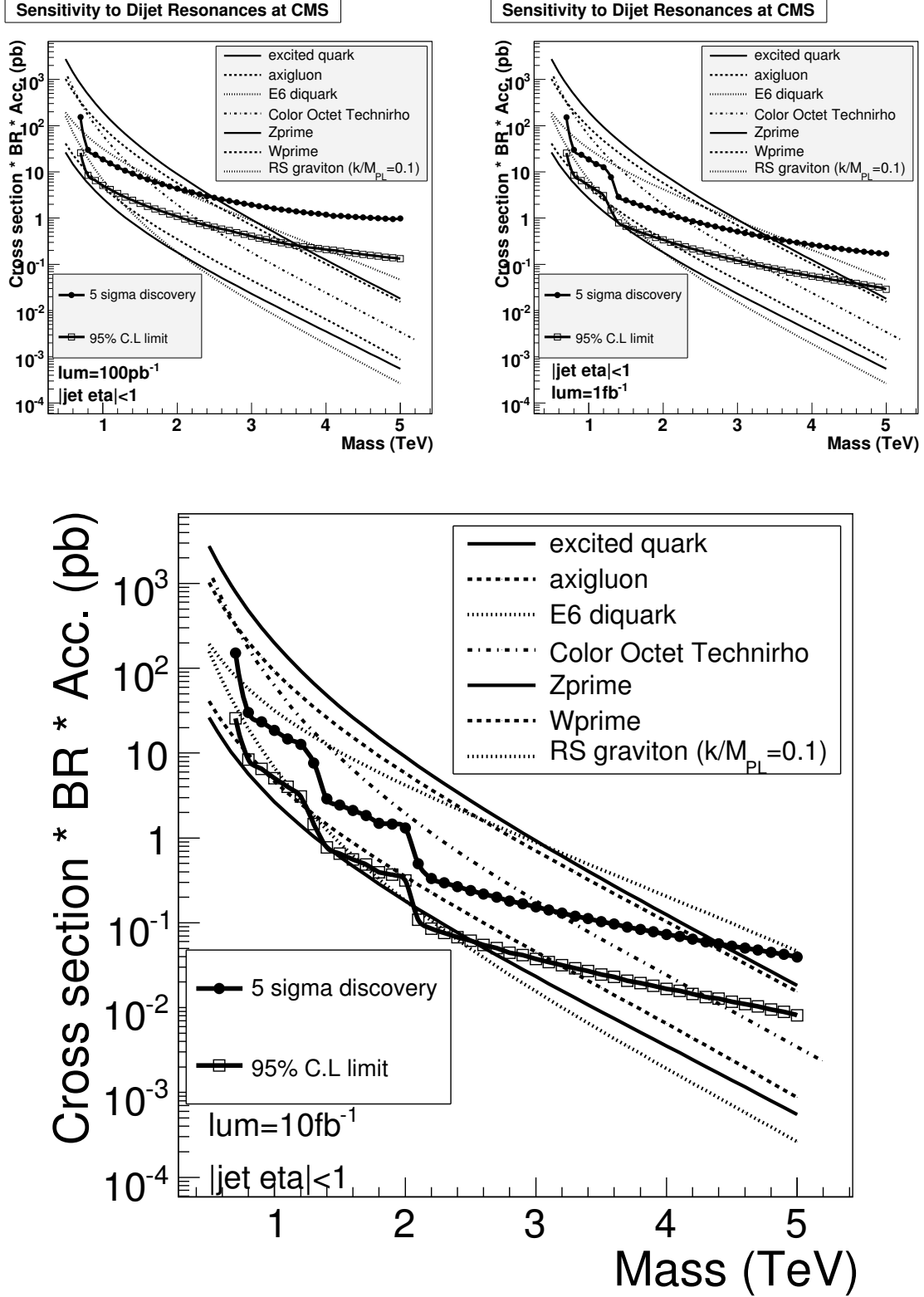


Figure 16: Dijet resonance sensitivity for 100 pb^{-1} (top left), 1 fb^{-1} (top right), and 10 fb^{-1} (bottom). The cross section of a resonance signal that could be discovered with 5σ significance (solid circles) or excluded at 95% CL (open boxes) is compared to the cross section for various resonance models. These sensitivities contain both statistical and systematic uncertainties.

Resonance Model	95% CL Excluded Mass (TeV/ c^2)			5 σ Discovered Mass (TeV/ c^2)		
	100 pb $^{-1}$	1 fb $^{-1}$	10 fb $^{-1}$	100 pb $^{-1}$	1 fb $^{-1}$	10 fb $^{-1}$
Excited Quark	0.7 - 3.6	0.7 - 4.6	0.7 - 5.4	0.7 - 2.5	0.7 - 3.4	0.7 - 4.4
Axigluon or Coloron	0.7 - 3.5	0.7 - 4.5	0.7 - 5.3	0.7 - 2.2	0.7 - 3.3	0.7 - 4.3
E_6 diquark	0.7 - 4.0	0.7 - 5.4	0.7 - 6.1	0.8 - 2.0	0.8 - 3.7	0.8 - 5.1
Color Octet Technirho	0.7 - 2.4	0.7 - 3.3	0.7 - 4.3	0.7 - 1.5	0.7 - 2.2	0.7 - 3.1
Randall-Sundrum Graviton	0.7 - 1.1	0.7 - 1.1	0.7 - 1.1	N/A	N/A	N/A
		1.3 - 1.6	1.3 - 1.6			
			2.1 - 2.3			
W'	0.8 - 0.9	0.8 - 0.9	0.8 - 1.0	N/A	N/A	N/A
		1.3 - 2.0	1.3 - 3.2			
Z'	N/A	N/A	2.1 - 2.5	N/A	N/A	N/A

Table 6: Sensitivity to dijet resonances with 100 pb $^{-1}$, 1 fb $^{-1}$, and 10 fb $^{-1}$. For each resonance model, we show the range of masses we expect to be able to exclude at a confidence level of 95% or greater, and the range of masses we expect to be able to discover with a significance of 5 σ or greater. All estimates are with both statistical and systematic uncertainties.

8 Conclusions

We have estimated the CMS sensitivity to narrow resonances in the dijet final state. This analysis is a simple search for bumps in the dijet mass distribution where both leading jets have $|\eta| < 1$. We have utilized a realistic jet trigger that was developed with this analysis in mind. It employs multiple jet thresholds and prescales allowing us to measure the dijet mass spectrum down to low masses where we overlap with Tevatron data. We determined our sensitivity using trigger tables for the three instantaneous luminosities, 10^{32} , 10^{33} and $10^{34} \text{ cm}^{-2} \text{ s}^{-1}$, and corresponding integrated luminosities of 100 pb^{-1} , 1 fb^{-1} and 10 fb^{-1} . For these samples we have determined our statistical sensitivity and have estimated our sensitivity in the presence of systematic uncertainties.

Our goal was to do as generic an analysis as possible, not concentrating on any particular model, but instead estimating our sensitivity to all models that give a narrow dijet resonance. The cross section for a narrow dijet resonance that CMS can expect to discovery at 5σ significance or exclude at 95% confidence level has been presented for each integrated luminosity and for each accessible resonance mass. These can be directly compared with the cross sections of any s – channel resonance that decays to two jets in the region $|\eta| < 1$.

We compare our cross section sensitivities with the expected cross section from models of excited quarks, axigluons, colorons, E_6 diquarks, color octet technirhos, W' , Z' , and Randall-Sundrum gravitons to determine the mass range for which we expect to be able to discover or exclude these models of dijet resonances. The mass ranges are listed in tab 6.

Clearly the size of the cross section is the determining factor in whether the model can be discovered. For excited quarks, axigluons, colorons, E_6 diquarks and color octet technirhos, we find that a 5σ discovery of a multi-TeV dijet resonance is possible for all luminosities considered. The first three models are produced via the color interaction, and E_6 diquarks are produced from the valence quarks of each proton, giving large cross sections. For W' , Z' , and Randall-Sundrum gravitons, we find that a 5σ discovery cannot be projected with confidence for any of the luminosities considered. The first two of these models employ electroweak couplings, and Randall-Sundrum gravitons are generally only considered likely for similar strengths of coupling, and all three of these models include one or more partons that are not valence quarks of the proton. Consequentially these models, while more popular among theorists, have smaller cross sections. Nevertheless, for all the models considered there is some range of mass we will be able to exclude at 95% CL if the data we take is in good agreement with QCD expectations.

We do not know what is the new physics beyond the standard model, but we know that something new must exist around the TeV scale. When CMS starts taking data we will prepared to search for TeV scale dijet resonances.

A Models and Calculations

This appendix contains details of the resonance models and a discussion of the lowest order calculation of their cross section. Code that calculates the cross section for the models was developed by us for CDF and used to publish limits [8]. Much of this appendix repeats prior CDF documentation of these calculations. We have repeated those calculations using CTEQ6L parton distributions [21] from LHAPDF [22]. The color octet technirho calculation uses Pythia, but it was also checked against against prior calculations published by CDF [8]. Each phenomena considered has a half-width at half maximum $\Gamma/2$ which is smaller than our dijet mass resolution. The resonance properties are summarized in table 7 and the cross sections are listed in table 9 and table 10.

Name	Symbol	Spin Parity (J^P)	Color Multiplet	$\Gamma/(2M)$	Channel
Axigluon	A	axial-vector (1^+)	octet	0.05	$q\bar{q}$
Coloron	C	vector (1^-)	octet	0.05	$q\bar{q}$
Excited Quark	q^*	fermion ($1/2^+$)	triplet	0.02	qg
Octet Technirho	ρ_{T8}	vector (1^-)	octet	0.01	$q\bar{q}, gg$
E_6 Diquark	D	scalar (0^+)	triplet	0.004	ud
Heavy W	W'	vector (1^-)	singlet	0.01	$q_1\bar{q}_2$
Heavy Z	Z'	vector (1^-)	singlet	0.01	$q\bar{q}$
RS Graviton	G	tensor (2^-)	singlet	0.01	$q\bar{q}, gg$

Table 7: Summary of Dijet Resonance Properties

A.1 Axigluons

In models of chiral color the unbroken color symmetry $SU(3)_C$ of QCD results from the breaking of the larger chiral color group $SU(3)_L \times SU(3)_R$. One prediction of all chiral color models is the axigluon, a massive color-octet of axial vector gluons. Axigluons are produced and decay strongly from quark-antiquark interactions, giving one of the largest cross section times branching ratio of any of the models considered.

A.1.1 Axigluon Lagrangian

The axigluon is constrained by gauge invariance to couple to all quark flavors according to the following interaction lagrangian:

$$\mathcal{L}_A = -ig_s t_{ij}^a \bar{q}^i \gamma_5 \gamma_\mu A^{\mu a} q^j \quad (5)$$

where t_{ij}^a are the usual $SU(3)$ color matrices. The axigluon cannot decay to two gluons because of parity conservation.

A.1.2 Width and Branching Ratio

The width of the axigluon is given by:

$$\Gamma_A = \frac{N_A \alpha_s M_A}{6} \quad (6)$$

where N_A counts the number of open decay channels: the number of quarks with mass less than the $M_A/2$. We will assume a standard model version of axigluons in which $M_A = 5$ when the axigluon has mass less than $2M_t$ and $M_A = 6$ when the axigluon has mass greater

than $2M_t$ but less than around a TeV. With this assumption $\Gamma_A/2 \approx .05M_A$. Additional families of quarks and leptons are required by this theory [23], but for convenience we will assume they have a mass greater than $M_A/2$. With these assumptions when $M_A < 2M_t$ the branching ratio to light quarks (u,d,s,c,b) is 1 and when $M_A > 2M_t$ the branching ratio is taken to be [24]:

$$BR(A \rightarrow q\bar{q}) = \frac{1}{5 + [1 - (2M_t/M_A)^2]^{3/2}} \quad (7)$$

A.1.3 Axigluon Cross Section

The total cross section for axigluon production is given by integrating the differential cross section in the narrow width approximation

$$\sigma = \int_{y_b^{min}}^{y_b^{max}} \frac{16\pi^2 \alpha_s}{9s} L(x_p, x_{\bar{p}}) A(y_b, y_{cut}, \cos \theta_{cut}^*) dy_b \quad (8)$$

where the minimum boost is $y_b^{min} = \max(-y_{cut}, \ln \sqrt{\tau})$, the maximum boost is $y_b^{max} = \min(y_{cut}, -\ln \sqrt{\tau})$, and $\tau = M^2/s = x_p x_{\bar{p}}$. The parton luminosity is given by

$$L(x_p, x_{\bar{p}}) = \sum_i (q_i(x_p) \bar{q}_i(x_{\bar{p}}) + \bar{q}_i(x_p) q_i(x_{\bar{p}})) \quad (9)$$

and $A(y_b, y_{cut}, \cos \theta_{cut}^*)$ is the acceptance for our jet rapidity and $\cos \theta^*$ cut which is evaluated at each value of y_b within the integral using the axial-vector decay angular distribution:

$$\frac{dN}{d \cos \theta^*} = 1 + \cos^2 \theta^* \quad (10)$$

This cross section is then multiplied by Eq. 7 to obtain the cross section times branching ratio we compare to our limit. This agrees with the results of reference [24] when evaluated with their cuts and parton distributions.

A.2 Colorons

In the flavor-universal coloron model [3], the strong gauge group is extended to $SU(3)_1 \times SU(3)_2$. The original gauge bosons from each $SU(3)$ mix to form a color octet of massless gluons and an color octet of massive colorons. The gluons interact with quarks through a conventional QCD coupling with strength g_s . The colorons ($C^{\mu a}$) interact with quarks through a new QCD-like coupling

$$\mathcal{L} = -g_g \cot \theta J_\mu^a C^{\mu a} \quad (11)$$

where J_μ^a is the color current

$$\sum_f \bar{q}_f \gamma_\mu \frac{\lambda^a}{2} q_f \quad (12)$$

where $\cot \theta$ is the mixing parameter of the two $SU(3)$ which is expected to have a value $\cot \theta \geq 1$. The colorons decay to all sufficiently light quarks; assuming there are n flavors lighter than $M_c/2$, the decay width is

$$\Gamma_c \approx \frac{n}{6} \alpha_s \cot^2 \theta M_c \quad (13)$$

The flavor universal coloron is thus a massive gluon which couples equally to all quarks. It is apparent that for the value of mixing $\cot \theta = 1$ the coloron has the same width as the axigluon, the same coupling strength to quarks as the axigluon, and the same production cross sections times branching ratio for jets. This follows from the similarity of the axial-vector and vector interactions and is also noted in reference [3]. The axigluon cross section discussed in the previous section is used for colorons with $\cot \theta = 1$ as well.

A.3 E_6 Diquarks

Superstring theory in 10 dimensions is anomaly free if the gauge group is $E_8 \times E_8$. The compactification of the extra 6 dimensions can lead to E_6 as the grand unification group for the strong and electroweak interactions. The E_6 models contain color triplet scalar diquarks $D(D^c)$ with charge $-1/3(+1/3)$ which couple to $\bar{u}\bar{d}(ud)$.

A.3.1 E_6 Diquark Lagrangian

The interaction lagrangian for transitions between E_6 diquarks and up and down quarks is [23]:

$$\mathcal{L}_D = \lambda \epsilon_{ijk} \bar{u}^i \frac{1 - \gamma_5}{2} d^j D^k + \frac{\lambda_c}{2} \epsilon_{ijk} \bar{u}^i \frac{1 + \gamma_5}{2} d^j D^c k + h.c. \quad (14)$$

where it is commonly assumed that the unknown couplings are of electromagnetic strength ($\lambda = \lambda_c = e$) and that the masses are degenerate ($M_{D^c} = M_D$).

A.3.2 E_6 Diquark Width and Branching Ratio

Assuming electromagnetic strength Yukawa couplings, the width of the E_6 diquarks is given by [4]:

$$\Gamma_D = \alpha M_D, \quad \Gamma_{D^c} = \alpha M_{D^c}/4 \quad (15)$$

where $\alpha = \lambda^2/4\pi$ is the electromagnetic coupling constant which is $1/128$ after running to high masses. E_6 diquarks in the first family decay into u and d quarks only.

A.3.3 E_6 Diquark Cross Section Calculation

The E_6 diquark cross section is obtained from integrating the subprocess differential cross sections over the Breit-Wigner resonance. Following reference [1], the differential cross section for D is given by:

$$\frac{d^2\sigma}{dx_p dx_{\bar{p}}} = \frac{\hat{s}}{108\pi} \frac{16\lambda}{(\hat{s} - M_D^2)^2 + \Gamma_D^2 M_D^2} [\bar{u}(x_p) \bar{d}(x_{\bar{p}}) + \bar{u}(x_{\bar{p}}) \bar{d}(x_p)] P \quad (16)$$

and similarly for \bar{D} with $\bar{q} \rightarrow q$ in the parton distributions. The cross section for D^c is given by

$$\frac{d^2\sigma}{dx_p dx_{\bar{p}}} = \frac{s_{hat} \alpha}{108\pi} \frac{\lambda}{(\hat{s} - M_{D^c}^2)^2 + \Gamma_{D^c}^2 M_{D^c}^2} (u(x_p) d(x_{\bar{p}}) + u(x_{\bar{p}}) d(x_p)) P \quad (17)$$

and similarly for \bar{D}^c with $q \rightarrow \bar{q}$ in the parton distributions. In Eq. 16 and 17, $\hat{s} = s x_p x_{\bar{p}}$ and the variable P is the kinematic acceptance which is discussed below. We find it more convenient to integrate over the variables $m = \sqrt{\hat{s}}$ and $y_b = (y_1 + y_2)/2 = (1/2) \ln(x_p/x_{\bar{p}})$ rather than x_p and $x_{\bar{p}}$, so we transform to these variables using $dm dy_b = (s/2m) dx_{\bar{p}} dx_p$ and

then integrate Eq. 16 and Eq. 17 from y_b^{min} to y_b^{max} to obtain the Breit-Wigner $d\sigma/dm$ for the diquark resonance. In this integral the kinematic acceptance is

$$P = P(y^{cut}, \cos\theta^*) \quad (18)$$

which is the probability that both final state partons pass our cuts in rapidity and $\cos\theta^* = \tanh(y^*) = \tanh(y_1 - y_2)$ as a function of the variable y_b . We had to work out the function P , essentially our acceptance for the excited quark decay given our kinematic cuts. This was an exercise in defining the boundaries in the y^* vs. y_b plane formed by our cuts, and then integrating the isotropic decay angular distribution from y_{min}^* to y_{max}^* at the given value of y_b . Finally, we integrated over the Breit-Wigner resonance to obtain the total cross section for an E_6 diquark, which includes D and D^c and their antiparticles. We checked our total cross section against the figure in reference [25] using the same cuts, parton distributions, and assumptions of that reference and they agreed to within 10%.

A.4 Excited Quarks

If quarks are composite particles then excited states are expected. As in reference [1] we only consider the simplest kind of excited quark, one with spin 1/2 and weak isospin 1/2.

A.4.1 Excited Quark Lagrangian

The Lagrangian for transitions between an excited quark of mass M^* and a quark plus a gauge boson ($q^* \leftrightarrow q + [\gamma, g, W, Z]$) is constrained by gauge invariance to be of magnetic moment type [1]:

$$\mathcal{L} = \frac{1}{2M^*} \bar{q}_R^* \sigma^{\mu\nu} (g_s f_s \frac{\lambda_a}{2} G_{\mu\nu}^a + g f \frac{\tau}{2} W_{\mu\nu} + g' f' \frac{Y}{2} B_{\mu\nu}) q_L + h.c. \quad (19)$$

where $G_{\mu\nu}^a$, $W_{\mu\nu}$, and $B_{\mu\nu}$ are the field-strength tensors of the gluon, the SU(2) and the U(1) gauge fields, Y is the weak hypercharge, and g_s , g and g' are the gauge coupling constants. Finally f_s , f and f' are unknown deviations of the couplings from their standard model values, determined by the composite dynamics, and are all assumed to be equal to one corresponding to no deviation from the standard model.

A.4.2 Excited Quark Width and Branching Ratios

Production of a single excited quark will take place in hadronic collisions via quark gluon fusion, this is clear from inspection of Eq. 19. The excited quark can then decay into a common quark and any gauge boson. The relative decay rates [1] are listed in Table 8 assuming standard model couplings.

Decay Mode	Br. Ratio(%)	Decay Mode	Br. Ratio(%)
$u^* \rightarrow ug$	83.4	$d^* \rightarrow dg$	83.4
$u^* \rightarrow u\gamma$	2.2	$d^* \rightarrow d\gamma$	0.5
$u^* \rightarrow dW$	10.9 ($e\nu$ 1.2)	$d^* \rightarrow uW$	10.9 ($e\nu$ 1.2)
$u^* \rightarrow uZ$	3.5 (ee .27)	$d^* \rightarrow dZ$	5.1 (ee .39)

Table 8: The decay modes and branching ratios of excited up and down quarks for $f_s = f = f'$ and $\alpha_s = 0.1$.

Expressions for the partial decay rates are given in reference [1]. The q^* half width for $f_s = f = f'$ is approximately given by

$$\frac{\Gamma(q^*)}{2} \approx 0.02 f^2 M^*. \quad (20)$$

which for $f \leq 1$ is significantly narrower than our dijet mass resolution.

A.4.3 Excited Quark Cross Section Calculation

The q^* total cross section is obtained by first explicitly calculating the Breit-Wigner differential cross section versus dijet mass, m , and then integrating over m . Following reference [1], the differential cross section is given by:

$$\frac{d\sigma}{dm} = \frac{2}{m} \int_{y_b^{min}}^{y_b^{max}} dy_b \tau \mathcal{L}(x_1, x_2) \hat{\sigma}(m^2) P \quad (21)$$

Here τ is related to the initial state parton fractional momenta x_1 and x_2 by $\tau = x_1 x_2 = m^2/s$. The kinematic variable y_b is given by $y_b = (y_{JET1} + y_{JET2})/2 = (1/2) \ln(x_1/x_2)$, and rapidity y and pseudorapidity η are equal because massless partons are assumed. The partonic “luminosity function” is just the product of parton distribution function:

$$\mathcal{L}(x_1, x_2) = q(x_1, m^2)g(x_2, m^2) + g(x_1, m^2)q(x_2, m^2) \quad (22)$$

Reference [1] states that “ u^* and d^* should, to a good approximation, be degenerate in mass”, and therefore the quark structure function is given by the sum of up, down, anti-up and anti-down parton distributions: $q = u + d + \bar{u} + \bar{d}$. Here we have used CTEQ6L [21] parton distributions.

The subprocess cross section is given by the following Breit-Wigner like resonance formula for an excited quark of mass M^* :

$$\hat{\sigma}(m^2) = \pi \frac{\hat{\Gamma}^2(qg \rightarrow q^*) \hat{\Gamma}(q^* \rightarrow qg)}{(m^2 - M^{*2})^2 + \hat{\Gamma}^2(q^*) M^{*2}} \quad (23)$$

where $\hat{\Gamma}(q^*)$, is the full width of the q^* resonance from all decay channels, and $\hat{\Gamma}(qg \rightarrow q^*)$ is approximately the partial width in the qg channel. As discussed in reference [1] the partial widths also contains a form factor and the kinematic factor (m/M^{*2}) to give the correct relativistic behavior off the resonance peak. The full expressions for these widths are too detailed to record here, but they can be found in reference [1]. The final variable in Eq. 21 is

$$P = P(\tau, y_b, P_T^{cut}, y_{JET}^{cut}, y^{*,cut}) \quad (24)$$

which is the probability that both final state partons pass our cuts in rapidity and P_T as a function of the variables τ and y_b . We had to work out the function P , essentially our acceptance for the excited quark decay given our kinematic cuts. This was an exercise in defining the boundaries in the y^* vs. y_b plane formed by our cuts, and then integrating the isotropic decay angular distribution from y_{min}^* to y_{max}^* at the given value of y_b .

After coding all this up we checked our calculation against the figures in reference [1]. We used the same cuts and center-of-mass collision energy and parton distributions chosen in that reference, and we got the same result to within about 10%.

A.5 Color Octet Technirhos

Color octet technirhos exist in models of either extended technicolor or topcolor-assisted technicolor [5]. They are produced via a vector-meson dominance model of mixing between the gluon and the color octet technirho ($q\bar{q}, gg \rightarrow g \rightarrow \rho_{T8}$). This mixing has the effect of reducing the cross section somewhat from what is expected for a normal color-interaction, like from axigluons or colorons. This mixing also moves the mass of the resonance off of its pole value by a few percent, making the mean observed $\sqrt{\hat{s}}$ of any color octet technirho resonance always at least a few percent higher than the pole mass. This mixing also means that the signal cross section is never modeled in isolation from QCD. Instead the QCD gluon propagator in the intermediate state is replaced by the inverse of a matrix containing gluons, multiple technirhos and its own colorons. The model's phenomenology is potentially quite complex, with multiple overlapping mass bumps and deviations of the QCD spectrum. We have chosen a set of parameters of the model that simplify the phenomenology to conform with our generic search.

We have used Pythia 6.321 to simulate the lowest order cross section at generator level for color octet technirhos decaying to dijets. We had numerous discussions with the author's of reference [5], and developed a set of straw-man parameters that would be reasonable for both the LHC and Tevatron. Inspired by "Benchmark V - Universal TC2 jets with large M V8" on page 32 of reference [5], the goal was to produce a single resonance in the dijet mass spectrum as a simple benchmark to search for. The value of the parameters which can all be set in Pythia are

1. Standard Topcolor-Assisted-Technicolor (TC2) couplings
2. Degenerate Technirhos: $M(\rho_{11}) = M(\rho_{12}) = M(\rho_{21}) = M(\rho_{22}) = M(\rho)$ the pole mass.
3. Mixing among the technirhos: $M'_8 = 0$ to reduce the mass shift from the pole mass.
4. Octet Technipion mass: $M(\pi_{22}^8) = 5M(\rho)/6$ to prevent $\rho \rightarrow \pi\pi$.
5. Singlet Technipion mass: $M(\pi_{22}^1) = M(\pi_{22}^8)/2$
6. Coloron Mass: $M(V8) = 100$ TeV coloron at "infinity" so it doesn't affect cross section.
7. Parameter $M_8 = 5M(\rho)/6$ which keeps $\rho \rightarrow g\pi$ small to avoid a large ρ width.

With these parameters we ran Pythia to obtain the \hat{s} distributions in the region of the technirho pole mass. There is always a single resonance near $\sqrt{\hat{s}} = 1.05M(\rho)$, with a full width of about $\Gamma = 0.01M(\rho)$. The shift of 5% in the observed mass from the pole mass is primarily due to the production mechanism which involves mixing with the gluon. The process is always simulated in the presence of QCD background because the color octet ρ is only produced by mixing with the s-channel gluon of the QCD background process. To obtain a signal cross section the QCD background was subtracted. To do this we fit the logarithm of the QCD background to a straight line vs mass in the sideband regions, $0.9M(\rho) < m < M(\rho)$ and $1.1M(\rho) < m < 1.2M(\rho)$, and subtracted this background from the signal region $M(\rho) < m < 1.1M(\rho)$. We binned the generated data in bins that are 0.5% of $M(\rho)$. The peak is the highest bin in the signal region after background subtraction. The signal is the peak bin, plus the 4 bins before the peak bin, plus the 8 bins after the peak bin. We required the two outgoing partons (jets) to each have $|\eta| < 1$. This gave us a total resonance cross section as a function of the mean $\sqrt{\hat{s}}$ which we show in table 9.

We produced technirho cross sections for both the Tevatron and the LHC. The ones for the Tevatron were in good agreement with prior analytic calculations we did for the Tevatron [13]. We have abandoned the analytic calculations because the author's of reference [5] have requested that we instead use their full model in Pythia. However, after our choice of parameters above, the two models are essentially the same.

M(pole) (GeV)	M (GeV)	Cross Section (pb)	Error (pb)
500.	525	1.16E+03	3.3E+01
700.	733	2.58E+02	7.4E+00
1000.	1045	5.03E+01	1.4E+00
1500.	1565	7.18E+00	1.9E-01
2000.	2086	1.55E+00	4.2E-02
3000.	3121	1.41E-01	4.0E-03
4000.	4155	1.79E-02	5.6E-04
5000.	5192	2.36E-03	9.1E-05
6000.	6224	3.02E-04	1.5E-05
7000.	7275	4.22E-05	2.5E-06
8000.	8318	5.77E-06	3.6E-07

Table 9: Cross Section for Color Octet Technirhos decay to dijets in $|\eta| < 1$. As a function of the pole mass we list the mean mass of the resonance, $M = \sqrt{\hat{s}}$, the cross section for the resonance decaying to two partons each in the region $|\eta| = 1$, and our statistical error on that cross section.

A.6 W' and Z'

We calculate cross sections for the W' and Z' of the Sequential Standard Model variety. Here we assume the W' has the same production cross section as the W (with M_W replaced by $M_{W'}$) and the same fractional width as the W . The same relations holds between the Z' and the Z . We use the subprocess cross section expression for W and Z production in reference [7] with the Fermi constant, G_F , replaced by

$$G'_F = G_F \left(\frac{M}{M'} \right)^2 \quad (25)$$

where M is the mass of the W or Z and M' is the mass of the W' or Z' respectively. Following Tevatron practice, we multiply the lowest order standard model cross sections by the following K factors to take into account higher order terms. The K factor for the W' is given by

$$K = 1 + \frac{8\pi\alpha_s}{9} \quad (26)$$

and the K factor for the Z' is

$$1 + \frac{\alpha_s}{2\pi} \frac{4}{3} \left(1 + \frac{4}{3}\pi^2 \right) \quad (27)$$

and both K factors are roughly 1.3. The total cross section is then calculated in the narrow width approximation. The angular decay distribution of these vector particles is handled in the same way as for the Axigluon previously discussed. The half width of the W'

$$\frac{\Gamma}{2} = \frac{2 \text{ GeV}}{2} \frac{M'_W}{M_W} \quad (28)$$

and the half width of the Z'

$$\frac{\Gamma}{2} = \frac{2.5 \text{ GeV}}{2} \frac{M'_Z}{M_Z} \quad (29)$$

are significantly less than our dijet mass resolution. The branching ratio for W' and Z' in the dijet channel is equal to the branching ratio to quarks other than the top quark.

A.7 Randall Sundrum Gravitons

In the Randall-Sundrum model there exists massive spin-2 gravitons which are Kaluza-Klein resonances that result from the compactified extra dimension. There are effectively only two parameters in the model. The choice of parameters of most phenomenological interest are the mass, M , of the lightest graviton resonance, G , and a coupling strength parameter k/\bar{M}_{PL} . Our cross sections are calculated for $k/\bar{M}_{PL} = 0.1$

In the narrow width approximation, the lowest order differential cross section for the production of a spin-2 graviton resonance of mass M and width Γ per unit of center-of-mass scattering angle $\cos \theta$ and boost η is given by [26]

$$\frac{d\sigma}{d\cos\theta d\eta_B} = \frac{1}{C_i} \left(\frac{2M}{s} \frac{\pi}{2} \Gamma \right) \left(\frac{20\pi}{M^2} B_i B_f \frac{1}{C_i} \right) F(\cos\theta^*) f(x_p) f(x_{\bar{p}}) \quad (30)$$

where the boost $\eta_B = (\eta_1 + \eta_2)/2$ is the average pseudorapidity of the final state partons (jets), s is the square of the proton-antiproton collision energy, C_i is the color of the initial state (3 for $q\bar{q}$ and 8 for gg), B_i and B_f are the branching fractions for the initial state and the final state respectively, $f(x_p)$ and $f(x_{\bar{p}})$ are the parton distributions of the initial state, and $F(\cos\theta)$ are the normalized angular distributions of the sub-process:

$$F(gg \rightarrow G \rightarrow q\bar{q}) = F(q\bar{q} \rightarrow G \rightarrow gg) = \frac{5}{8}(1 - \cos^4\theta) \quad (31)$$

$$F(gg \rightarrow G \rightarrow gg) = \frac{5}{32}(1 + 6\cos^2\theta + \cos^4\theta) \quad (32)$$

$$F(q\bar{q} \rightarrow G \rightarrow q\bar{q}) = \frac{5}{8}(1 - 3\cos^2\theta + 4\cos^4\theta) \quad (33)$$

In equation 30 our theoretical colleague has provided us with the cross section for a Breit-Wigner narrow resonance suitably weighted by the initial and final state branching fractions [25]. The final state branching fractions are given by the ratio of the partial widths to the full widths, where the partial width [6] for photons is

$$\Gamma(G \rightarrow \gamma\gamma) = \frac{2x_1^2}{160\pi} \left(\frac{k}{\bar{M}_{Pl}} \right)^2 M \quad (34)$$

for gluons is

$$\Gamma(G \rightarrow gg) = \frac{2x_1^2}{20\pi} \left(\frac{k}{\bar{M}_{Pl}} \right)^2 M \quad (35)$$

for each variety of lepton is

$$\Gamma(G \rightarrow l\bar{l}) = \frac{2x_1^2}{320\pi} \left(\frac{k}{\bar{M}_{Pl}} \right)^2 M \quad (36)$$

for each variety of light quark (u,d,s,c or b) is

$$\Gamma(G \rightarrow q\bar{q}) = \frac{6x_1^2}{320\pi} \left(\frac{k}{M_{Pl}} \right)^2 M \quad (37)$$

for the top quark is

$$\Gamma(G \rightarrow t\bar{t}) = \frac{6x_1^2}{320\pi} \left(\frac{k}{M_{Pl}} \right)^2 M \left(1 - \frac{4m_t^2}{M^2} \right)^{3/2} \left(1 + \frac{8m_t^2}{3M^2} \right) \quad (38)$$

for the W boson is

$$\Gamma(G \rightarrow W^+W^-) = \frac{2x_1^2}{80\pi} \left(\frac{k}{M_{Pl}} \right)^2 M \left(1 - \frac{4m_W^2}{M^2} \right)^{3/2} \left(\frac{13}{12} + \frac{14m_W^2}{3M^2} + \frac{4m_W^4}{M^2} \right) \quad (39)$$

and for the Z boson is

$$\Gamma(G \rightarrow ZZ) = \frac{x_1^2}{80\pi} \left(\frac{k}{M_{Pl}} \right)^2 M \left(1 - \frac{4m_Z^2}{M^2} \right)^{3/2} \left(\frac{13}{12} + \frac{14m_Z^2}{3M^2} + \frac{4m_Z^4}{M^2} \right) \quad (40)$$

The full width Γ is the sum of the partial widths. For $\frac{k}{M_{Pl}} = 0.1$, the percent width Γ/M is about 1%. The final state branching fractions B_f are just the partial widths divided by the full width. The initial state branching fractions for quarks are identical to the final state branching fractions for quarks. The initial state branching fractions for gluons are twice the final state branching fractions for gluons, to remove a factor of 1/2 for identical particles in the final state [26]. Other differences between initial state and final state spin and color statistics have already been accounted for in equation 30.

The differential cross section in Eq 30 gives the same expression for graviton decays as can be found in the literature [6].

The total cross section at lowest order is given by the integration

$$\sigma = \int \int \frac{d\sigma}{d \cos \theta d\eta_B} d \cos \theta d\eta_B \quad (41)$$

over the angular range and the pseudorapidity boost range defined by our jet eta cuts, $|\eta_1| < \eta_{cut}$ and $|\eta_2| < \eta_{cut}$, and the fractional momentum of the partons, $\max(-\eta_{cut}, \ln \sqrt{\tau}) < \eta < \min(\eta_{cut}, -\ln \sqrt{\tau})$, where $\tau = M^2/s = x_p x_{\bar{p}}$, where in our search $\eta_{cut} = 1$.

We checked our calculation for Randall-Sundrum gravitons decaying to dijets against that from Pythia. We made this comparison in 2003 when Pythia used an incorrect angular distribution for Graviton decays to bosons (isotropic). To have a valid comparison we simply compared our calculation to Pythia without any angular cuts and got identical results to within a few percent.

Mass (GeV)	q^* (pb)	A or C (pb)	D (pb)	Z' (pb)	W' (pb)	G (pb)
500	0.2760E+04	0.1018E+04	0.1935E+03	0.2634E+02	0.4092E+02	0.1581E+03
600	0.1416E+04	0.5467E+03	0.1208E+03	0.1464E+02	0.2349E+02	0.7131E+02
700	0.7954E+03	0.3225E+03	0.8113E+02	0.8858E+01	0.1461E+02	0.3573E+02
800	0.4776E+03	0.2032E+03	0.5737E+02	0.5697E+01	0.9610E+01	0.1935E+02
900	0.3016E+03	0.1345E+03	0.4215E+02	0.3833E+01	0.6593E+01	0.1113E+02
1000	0.1981E+03	0.9240E+02	0.3189E+02	0.2669E+01	0.4671E+01	0.6719E+01
1100	0.1343E+03	0.6536E+02	0.2469E+02	0.1911E+01	0.3394E+01	0.4219E+01
1200	0.9347E+02	0.4732E+02	0.1947E+02	0.1398E+01	0.2517E+01	0.2738E+01
1300	0.6646E+02	0.3492E+02	0.1558E+02	0.1041E+01	0.1897E+01	0.1828E+01
1400	0.4812E+02	0.2618E+02	0.1262E+02	0.7874E+00	0.1450E+01	0.1250E+01
1500	0.3539E+02	0.1989E+02	0.1032E+02	0.6029E+00	0.1121E+01	0.8724E+00
1600	0.2637E+02	0.1528E+02	0.8517E+01	0.4666E+00	0.8755E+00	0.6202E+00
1700	0.1988E+02	0.1186E+02	0.7078E+01	0.3644E+00	0.6892E+00	0.4481E+00
1800	0.1514E+02	0.9274E+01	0.5917E+01	0.2868E+00	0.5464E+00	0.3283E+00
1900	0.1164E+02	0.7306E+01	0.4973E+01	0.2273E+00	0.4358E+00	0.2436E+00
2000	0.9011E+01	0.5792E+01	0.4197E+01	0.1813E+00	0.3494E+00	0.1828E+00
2100	0.7027E+01	0.4617E+01	0.3556E+01	0.1453E+00	0.2814E+00	0.1385E+00
2200	0.5514E+01	0.3698E+01	0.3023E+01	0.1170E+00	0.2275E+00	0.1059E+00
2300	0.4350E+01	0.2974E+01	0.2577E+01	0.9459E-01	0.1846E+00	0.8162E-01
2400	0.3449E+01	0.2402E+01	0.2202E+01	0.7676E-01	0.1501E+00	0.6336E-01
2500	0.2747E+01	0.1946E+01	0.1886E+01	0.6249E-01	0.1225E+00	0.4950E-01
2600	0.2197E+01	0.1581E+01	0.1618E+01	0.5102E-01	0.1001E+00	0.3889E-01
2700	0.1763E+01	0.1288E+01	0.1390E+01	0.4176E-01	0.8194E-01	0.3072E-01
2800	0.1420E+01	0.1052E+01	0.1196E+01	0.3425E-01	0.6719E-01	0.2438E-01
2900	0.1146E+01	0.8605E+00	0.1030E+01	0.2816E-01	0.5516E-01	0.1943E-01
3000	0.9281E+00	0.7055E+00	0.8876E+00	0.2318E-01	0.4533E-01	0.1554E-01
3100	0.7533E+00	0.5793E+00	0.7657E+00	0.1912E-01	0.3729E-01	0.1248E-01
3200	0.6127E+00	0.4763E+00	0.6610E+00	0.1579E-01	0.3068E-01	0.1005E-01
3300	0.4994E+00	0.3922E+00	0.5708E+00	0.1306E-01	0.2526E-01	0.8112E-02
3400	0.4077E+00	0.3233E+00	0.4931E+00	0.1081E-01	0.2081E-01	0.6565E-02
3500	0.3334E+00	0.2667E+00	0.4262E+00	0.8954E-02	0.1714E-01	0.5325E-02
3600	0.2731E+00	0.2202E+00	0.3683E+00	0.7424E-02	0.1411E-01	0.4328E-02
3700	0.2239E+00	0.1820E+00	0.3183E+00	0.6160E-02	0.1162E-01	0.3523E-02
3800	0.1838E+00	0.1504E+00	0.2751E+00	0.5113E-02	0.9567E-02	0.2873E-02
3900	0.1511E+00	0.1244E+00	0.2378E+00	0.4246E-02	0.7873E-02	0.2345E-02
4000	0.1243E+00	0.1030E+00	0.2054E+00	0.3527E-02	0.6475E-02	0.1917E-02
4100	0.1023E+00	0.8522E-01	0.1774E+00	0.2931E-02	0.5322E-02	0.1569E-02
4200	0.8429E-01	0.7054E-01	0.1532E+00	0.2435E-02	0.4371E-02	0.1284E-02
4300	0.6949E-01	0.5840E-01	0.1323E+00	0.2024E-02	0.3587E-02	0.1053E-02
4400	0.5732E-01	0.4834E-01	0.1141E+00	0.1682E-02	0.2941E-02	0.8631E-03
4500	0.4730E-01	0.4001E-01	0.9841E-01	0.1397E-02	0.2408E-02	0.7080E-03
4600	0.3905E-01	0.3312E-01	0.8481E-01	0.1160E-02	0.1970E-02	0.5810E-03
4700	0.3225E-01	0.2740E-01	0.7305E-01	0.9635E-03	0.1610E-02	0.4768E-03
4800	0.2664E-01	0.2266E-01	0.6288E-01	0.7998E-03	0.1314E-02	0.3914E-03
4900	0.2201E-01	0.1873E-01	0.5408E-01	0.6635E-03	0.1071E-02	0.3213E-03
5000	0.1819E-01	0.1548E-01	0.4648E-01	0.5501E-03	0.8717E-03	0.2637E-03
5500	0.7004E-02	0.5901E-02	0.2150E-01	0.2132E-03	0.3039E-03	0.9767E-04
6000	0.2684E-02	0.2194E-02	0.9677E-02	0.8044E-04	0.1012E-03	0.3555E-04
6500	0.1017E-02	0.7874E-03	0.4209E-02	0.2923E-04	0.3192E-04	0.1255E-04
7000	0.3792E-03	0.2695E-03	0.1756E-02	0.1011E-04	0.9494E-05	0.4245E-05
7500	0.1386E-03	0.8693E-04	0.6969E-03	0.3291E-05	0.2661E-05	0.1358E-05
8000	0.4954E-04	0.2610E-04	0.2604E-03	0.9947E-06	0.7087E-06	0.4051E-06

Table 10: Cross Section for dijet resonances with jet pseudorapidity $|\eta| < 1$.

B References

- [1] U. Baur, I. Hinchliffe, and D. Zeppenfeld, *excited quark production at hadron colliders*, Int. J. Mod. Phys.A2, 1285 (1987), Fermilab-Conf-87-102-T. Also U. Baur, M. Spira and P. M. Zerwas, *Excited-quark and -lepton production at hadron colliders*, Phys. Rev. D42, 815 (1990).
- [2] J. Bagger, C. Schmidt, and S. King, *axigluon production in hadronic collisions*, Phys. Rev. D37, 1188 (1988).
- [3] E. Simmons, *Coloron Phenomenology*, Phys.Rev.D55,1678 (1997), hep-ph/9608269.
- [4] J. L. Hewett and T. G. Rizzo, *low-energy phenomenology of superstring inspired $e(6)$ models*, Phys.Rept.183,193 (1989); V.D. Angelopoulos, John R. Ellis, H. Kowalski, D.V. Nanopoulos, N.D. Tracas , F. Zwirner, *search for new quarks suggested by the superstring*, Nucl.Phys.B292, 59 (1987).
- [5] Kenneth Lane and Stephen Mrenna, *The collider phenomenology of technihadrons in the technicolor Straw Man Model*, Phys. Rev. D67,115011(2003), hep-ph/0210299.
- [6] L. Randall and R. Sundrum, *a large mass hierarchy from a small extra dimension*, Phys.Rev.Lett.83, 3370 (1999), hep-ph/9905221; J. Bijnens, P. Eerola, M. Maul, A. Mansson, T. Sjostrand, *qcd signatures of narrow graviton resonances in hadron colliders*, Phys.Lett.B503,341 (2001), hep-ph/0101316.
- [7] E. Eichten, I. Hinchliffe, Kenneth D. Lane, C. Quigg, *Super Collider Physics*, Rev.Mod.Phys.56:579-707 (1984).
- [8] CDF Collaboration, F. Abe et al., *Search for New Particles Decaying to Dijets at CDF*, Phys. Rev. D55: 5263-5268 (1997), hep-ex/9702004.
- [9] D0 Collaboration, V. M. Abazov et al., *Search for new particles in the two jet decay channel with the D0 detector*, Phys.Rev.D69: 111101 (2004), hep-ex/0308033.
- [10] Selda Esen and Robert M. Harris, *Jet Triggers and Dijet Mass*, CMS Note (2006).
- [11] A. Heister, O. Kodolova, V. Konopliankov, S. Petrushanko, J. Rohlf, C. Tully, A. Ulyanov, *"Measurement of Jets with the CMS Detector at the LHC"*, **CMS 2006/036**.
- [12] The RecJetRootTree code is in the ORCA 8.7.1 package at <http://cmsdoc.cern.ch/ORCA/>.
- [13] CDF Collaboration (T. Affolder et al.), *A Measurement of the Differential Dijet Mass Cross-Section in p anti- p Collisions at $\sqrt{s} = 1.8$ TeV*, Phys.Rev.D61:091101 (2000), hep-ex/9912022.
- [14] D0 Collaboration (B. Abbott et al.), *The dijet mass spectrum and a search for quark compositeness in anti- p p collisions at $\sqrt{s} = 1.8$ TeV*, Phys.Rev.Lett.82:2457-2462 (1999), hep-ex/9807014.
- [15] Selda Esen and Robert M. Harris, *CMS Sensitivity to Quark Contact Interactions*, CMS Note (2006).

- [16] Review of Particle Physics, Physics Letters B Vol.592,1-4(2004) 1-1110, statistics discussion online at <http://pdg.lbl.gov/2005/reviews/statrpp.pdf>.
- [17] CDF Collaboration (F. Abe et al.), *Search for New Particles Decaying to Dijets in p anti- p Collisions at $\sqrt{s} = 1.8$ TEV*, Phys.Rev.Lett.74:3538-3543 (1995), hep-ex/9501001.
- [18] A. L. Read, NIM A425, 357 (1999).
- [19] Robert M. Harris, *Discovery Mass Reach for Excited Quarks at Hadron Colliders*, FERMILAB-CONF-96-285-E, hep-ph/9609319.
- [20] CMS Collaboration, D. Acosta et al., **CMS Physics TDR Volume 1** CERN/LHCC 2006-001 (2006). Section 11.6.1: *Data-driven calibration strategy* beginning on page 421.
- [21] J. Pumplin et al., *New generation of parton distributions with uncertainties from global QCD analysis*, JHEP 07 (2002) 012, hep-ph/0201195.
- [22] LHAPDF code available online at <http://vircol.fnal.gov/>.
- [23] P. Frampton and S. Glashow, *Chiral Color: An Alternative to the Standard Model*, Phys. Lett. B190, 157 (1987).
- [24] G. Katsilieris, O. Korakiantitis and S. Vlassopoulos, *Two-jet rates affected by exotic particles at hadron colliders*, Glashow, Phys. Lett. B288(1992)221.
- [25] Thomas G. Rizzo, *Constraints on new physics from Fermilab Tevatron dijet data*, Physical Review D48,4470 (1993).
- [26] Tom Rizzo private communication on March 14, 2003.